

ACCEPTED MANUSCRIPT

# Understanding ultrasound neuromodulation using a computationally efficient and interpretable model of intramembrane cavitation

To cite this article before publication: Théo Lemaire *et al* 2019 *J. Neural Eng.* in press <https://doi.org/10.1088/1741-2552/ab1685>

## Manuscript version: Accepted Manuscript

Accepted Manuscript is “the version of the article accepted for publication including all changes made as a result of the peer review process, and which may also include the addition to the article by IOP Publishing of a header, an article ID, a cover sheet and/or an ‘Accepted Manuscript’ watermark, but excluding any other editing, typesetting or other changes made by IOP Publishing and/or its licensors”

This Accepted Manuscript is © 2018 IOP Publishing Ltd.

During the embargo period (the 12 month period from the publication of the Version of Record of this article), the Accepted Manuscript is fully protected by copyright and cannot be reused or reposted elsewhere.

As the Version of Record of this article is going to be / has been published on a subscription basis, this Accepted Manuscript is available for reuse under a CC BY-NC-ND 3.0 licence after the 12 month embargo period.

After the embargo period, everyone is permitted to use copy and redistribute this article for non-commercial purposes only, provided that they adhere to all the terms of the licence <https://creativecommons.org/licences/by-nc-nd/3.0>

Although reasonable endeavours have been taken to obtain all necessary permissions from third parties to include their copyrighted content within this article, their full citation and copyright line may not be present in this Accepted Manuscript version. Before using any content from this article, please refer to the Version of Record on IOPscience once published for full citation and copyright details, as permissions will likely be required. All third party content is fully copyright protected, unless specifically stated otherwise in the figure caption in the Version of Record.

View the [article online](#) for updates and enhancements.

# Understanding ultrasound neuromodulation using a computationally efficient and interpretable model of intramembrane cavitation

Théo Lemaire<sup>1</sup>, Esra Neufeld<sup>2</sup>, Niels Kuster<sup>2,3</sup>, and Silvestro Micera<sup>1,4</sup>

<sup>1</sup> Translational Neural Engineering Laboratory, Center for Neuroprosthetics and Institute of Bioengineering, School of Engineering, École Polytechnique Fédérale de Lausanne (EPFL), Lausanne, Switzerland  
<sup>2</sup> Foundation for Research on Information Technologies in Society (IT<sup>2</sup>S), Zurich, Switzerland  
<sup>3</sup> Department of Information Technology and Electrical Engineering, Swiss Federal Institute of Technology (ETH), Zurich, Zurich, Switzerland  
<sup>4</sup> The Biorobotics Institute, Scuola Superiore Sant'Anna (SSSA), Pisa, Italy

E-mail: [silvestro.micera@epfl.ch](mailto:silvestro.micera@epfl.ch)

## Abstract

**Objective.** Low-intensity focused ultrasound stimulation (LIFUS) emerges as an attracting technology for noninvasive modulation of neural circuits, yet the underlying action mechanisms remain unclear. The neuronal intramembrane cavitation excitation (NICE) model suggests that LIFUS excites neurons through a complex interplay between microsecond-scale mechanical oscillations of so-called sonophores in the plasma membrane and the development of a millisecond-scale electrical response. This model predicts cell-type-specific responses that correlate indirectly with experimental data, but it is computationally expensive and difficult to interpret, which hinders its potential validation. Here, we introduce a multi-Scale Optimized Neuronal Intramembrane Cavitation (SONIC) model to achieve fast, accurate simulations and confer interpretability in terms of effective electrical response. **Approach.** The NICE system is recast in terms of smoothly evolving differential variables affected by cycle averaged internal variables that are a function of sonophore size and charge density, stimulus frequency and pressure amplitude. Problem separation allows to precompute lookup tables for these functions, which are interpolated at runtime to compute coarse-grained, electrophysiologically interpretable and spatially distributed predictions of neural responses. **Main Results.** The SONIC model accelerates computation by more than three orders of magnitude, accurately captures millisecond-scale electrical responses of various cortical and thalamic neurons and offers an increased interpretability to the effects of ultrasonic stimuli in terms of effective membrane dynamics. Using this model, we explain how different spiking behaviors can be achieved in cortical neurons by varying LIFUS parameters, and interpret predictions of spike amplitude and firing rate in light of the effective electrical system. We demonstrate the substantial influence of sonophore size on excitation thresholds, and use a nanoscale spatially extended SONIC model to suggest that partial sonophore membrane coverage has a limited impact on neuronal excitability. **Significance.** By providing an electrophysiologically interpretable

description, the SONIC model clarifies cell-type-specific LIFUS neuromodulation according to the intramembrane cavitation hypothesis.

**Keywords:** Coarse-graining, Computational modeling, Electrophysiological interpretability, Intramembrane cavitation, Neural dynamics, Neuromodulation, Temporal multiscaling, Ultrasound stimulation

## 1. Introduction

Ultrasound (US)-based therapeutic applications, such as diagnostic imaging and thermal ablation therapies, are now widely accepted in the clinical field [1,2]. Low-intensity focused ultrasound stimulation (LIFUS), employing the same technology but with different sonication parameters (carrier frequency, peak pressure amplitude, duration, pulse repetition frequency, and duty cycle), has recently emerged as a very compelling modality for neuromodulation therapies. Owing to their mechanical nature, US waves can be accurately directed through biological tissue, offering the ability to concentrate the acoustic energy to a deep focal spot [2,3]. Moreover, numerous experiments on both animal models and humans have demonstrated that transcranial LIFUS is able to either excite, inhibit, or modulate the electrical activity of neurons in the central nervous system (CNS) [4–10]. Furthermore, exhaustive explorations of different sonication parameters on the motor cortex of mice have shown that stronger stimulus intensities and durations increase the probability of a motor response without affecting the duration or strength of the response, thereby suggesting a threshold excitation mechanism associated with the US intensity [6]. LIFUS could therefore trigger a local and controllable neuromodulatory effect on various neural targets, using a distant and possibly noninvasive sonication device. However, in order for LIFUS to become a reliable neuromodulation technology, we must elucidate the fundamental mechanism(s) by which US waves interact with neural tissue at the cellular scale, how these mechanisms may vary across neural structures and how optimal sonication parameters change with it.

Several theories have emerged to try to decipher this interaction. Among them, the neuronal intramembrane cavitation excitation (NICE) model [11] hypothesizes that incoming US waves induce the cavitation of specific nanometer-scale phospholipidic structures (so-called “bilayer sonophores”) within plasma membranes. This model provides quantitative predictions of cell-type-specific neural responses upon US exposure that result in excitation or inhibition of cortical networks depending on LIFUS parameters [12]. These predictions agree with the results of numerous in vitro experiments and in vivo studies sonicating the CNS of various animal models [5,6,13–16]. Yet, the model is purely theoretical and built around the intramembrane cavitation hypothesis, whose direct mechanical and electrical manifestations have yet to be observed experimentally. Moreover, the intrinsic electromechanical coupling of the model entails important computational limitations. From an algorithmic standpoint, the explicit modeling of mechanical membrane oscillations with microsecond-scale periodicity results in a very stiff differential system that

severely hinders numerical integration. From an analysis standpoint, the bidirectional coupling between mechanical and electrical variables evolving at different time scales produces a singular electrical response that can be difficult to interpret under the classical frame of neural dynamics. These limitations have so far prevented systematic, large-scale explorations of the LIFUS parameter space with the NICE electromechanical model, and its efficient integration in realistic applications involving the simultaneous solving of coupled differential systems, such as multi-compartmental morphological models and neuron population models.

In this study, we present a coarse-grained variant of the NICE electromechanical model – the so-called multi-Scale Optimized Neuronal Intramembrane Cavitation (SONIC) model – that allows the interpretation of the millisecond-scale dynamics of neural responses upon US exposure in terms of effective membrane dynamics. We show that the SONIC model can provide accurate predictions of cell-type-specific neural responses with respect to the detailed NICE model, while significantly decreasing computation times. We then exploit the SONIC model to explore systematically the dense, multidimensional LIFUS parameter space, and analyze responses of different neuron types with an advanced electrophysiological understanding. Finally, we use a nanoscale spatially extended SONIC model to study the impact of partial sonophore coverage on predicted neural responses and expected excitability.

## 2. Methods

### 2.1 The NICE electromechanical model

The NICE electromechanical model [11,12,17] is a mathematical model consisting of a system of first- and second-order differential equations describing the dynamic mechanical and electrical behavior of a bilayer sonophore that cavitates upon sonication while being anchored by surrounding transmembrane proteins (Figure 1(a)).

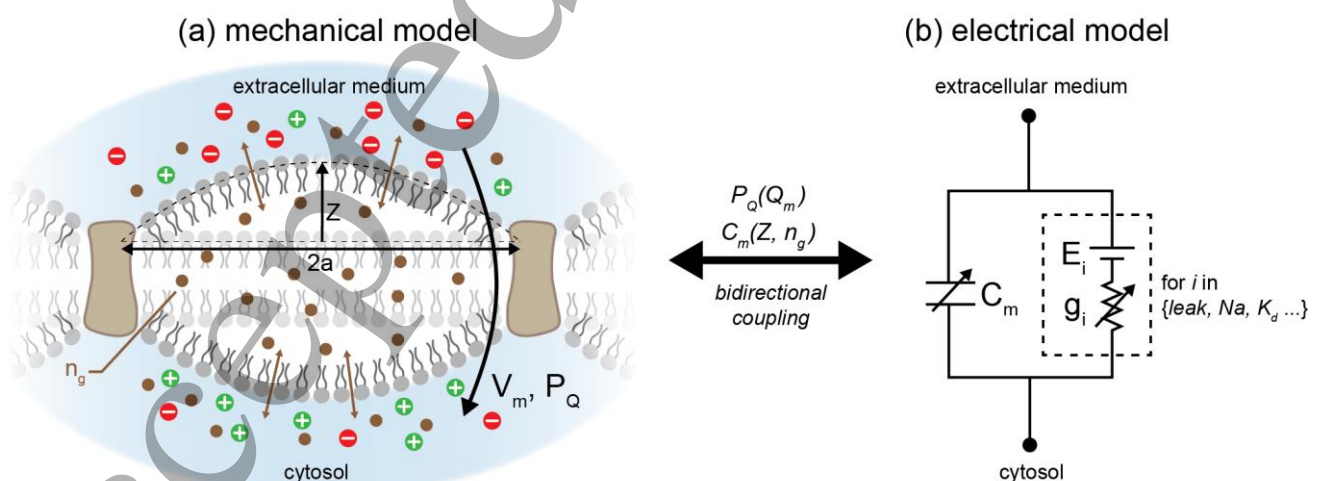


**Figure 1. Description of the NICE electromechanical model.** (a) Schematic representation of a bilayer sonophore structure (phospholipidic layers, inner cavity and surrounding transmembrane proteins) with the associated differential variables  $Z$  (apex deflection) and  $n_g$  (internal gas molar content). The local transmembrane potential  $V_m$  and electric pressure  $P_Q$  resulting from charge distributions on both sides of the membrane (green and red dots) are also indicated. (b) Electrical circuit representation of the local membrane dynamics, with the same transmembrane potential, a

deflection-dependent capacitance  $C_m$ , and cell-type-specific Hodgkin-Huxley ionic conductances and reversal potentials.

### 2.1.1 NICE mechanical model.

The mechanical part of the NICE electromechanical model predicts that incoming US waves generate a dynamic pressure imbalance that drives alternating expansions and compressions of sonophore structures, to oscillate at the US frequency. This cyclic behavior is captured by a second-order partial differential equation (akin to the Rayleigh-Plessey equation of bubble cavitation [18]) describing the antiphase apex deflection  $Z$  of the sonophore inner and outer leaflets, and a first-order equation describing the variation of internal gas content  $n_g$ :

$$\begin{aligned} \frac{d^2 Z}{dt^2} &= -\frac{3}{2R(Z)} \left( \frac{dZ}{dt} \right)^2 + \frac{1}{\rho_l \cdot |R(Z)|} \left[ P_A + P_S(Z) + P_{VS} \left( \frac{dZ}{dt} \right) - P_0 + P_{VL} \left( \frac{dZ}{dt} \right) + P_M(Z) + P_G(Z, n_g) + P_Q(Z, Q_m) \right] \\ \frac{dn_g}{dt} &= \frac{2S(Z) \cdot D_{gl}}{\xi} \left( C_g - \frac{P_G(Z)}{k_H} \right) \end{aligned} \quad (1)$$

where  $R(Z)$  and  $S(Z)$  represent the curvature radius and surface area of a sonophore leaflet and  $Q_m$  the local membrane charge density around the sonophore (for a definition of all other parameters see Table 1). Ultimately, the normal acceleration of a leaflet apex depends on the resultant of the applied acoustic pressure  $P_A$ , the constant hydrostatic pressure  $P_0$  around the membrane, and several intrinsic pressure forces, defined as in [11,17]:

- the elastic membrane tension pressure developed in the two leaflets:  $P_S(Z) = -\frac{k_S}{R(Z)} \frac{(S(Z)-S_0)}{S_0}$
- the viscous pressure developing in the leaflets:  $P_{VS} \left( \frac{dZ}{dt} \right) = -12 \frac{\mu_S \cdot \delta_0}{R^2(Z)} \frac{dZ}{dt}$
- the viscous pressure in the extra-membrane medium:  $P_{VL} \left( \frac{dZ}{dt} \right) = -4 \frac{\mu_l}{|R(Z)|} \frac{dZ}{dt}$
- the intermolecular pressure between leaflets:  $P_M(Z) = \frac{1}{S(Z)} \int_0^{2\pi} \int_0^a A_r \cdot (\gamma^x - \gamma^y) dr d\theta$  with  $\gamma = \frac{\Delta^*}{2z(r) + \Delta(Q_{m0})}$
- the internal gas pressure in the cavity:  $P_G(Z, n_g) = \frac{n_g \cdot R_g \cdot T}{V(Z)}$
- the electric pressure exerted on the sonophore by charges on either side of its membrane:  $P_Q(Z, Q_m) = -\frac{S_0}{S} \frac{Q_m^2}{2\epsilon_0 \cdot \epsilon_r}$

Here,  $S_0$  represents the leaflet surface area at rest,  $V(Z)$  the sonophore volume,  $r$  the in-plane distance from the sonophore center,  $z(r)$  the local deflection at this distance, and  $\Delta(Q_{m0})$  the charge-dependent gap between the two leaflets of the sonophore when the neuron is at rest (computed by canceling out  $P_M$  and  $P_Q$  at  $Z = 0$ ).

**Table 1. Parameters of the NICE mechanical model.**

Parameter	Symbol	Unit	Value	Source(s)
-----------	--------	------	-------	-----------

Sonophore radius (default value)	$a$	nm	32.0	[11]
Temperature	$T$	K	309.15	[19]
Universal gas constant	$R_g$	$\text{Pa}\cdot\text{m}^3\cdot\text{mol}^{-1}\cdot\text{K}^{-1}$	8.314	[20]
Thickness of the leaflet	$\delta_0$	nm	2.0	[17,21]
Gap between the two leaflets on an uncharged membrane	$\Delta^*$	nm	1.4	[17]
Intermolecular pressure coefficient	$A_r$	Pa	$10^5$	
Exponent in the intermolecular repulsion term	$x$	-	5.0	
Exponent in the intermolecular attraction term	$y$	-	3.3	[22]
Density of the extramembrane medium	$\rho_l$	$\text{kg}\cdot\text{m}^{-3}$	1075	
Dynamic viscosity of the extramembrane medium	$\mu_l$	$\text{Pa}\cdot\text{s}$	$7\cdot 10^{-4}$	[11]
Dynamic viscosity of the leaflet	$\mu_s$	$\text{Pa}\cdot\text{s}$	0.035	
Area compression modulus of the bilayer membrane	$k_s$	$\text{N}\cdot\text{m}^{-1}$	0.24	[17,23,24]
Gas concentration in the extra-membrane medium	$C_g$	$\text{mol}\cdot\text{m}^{-3}$	0.62	[11,25,26]
Henry's constant	$k_H$	$\text{Pa}\cdot\text{m}^3\cdot\text{mol}^{-1}$	$1.613\cdot 10^5$	
Hydrostatic pressure in the extra-membrane medium	$P_0$	Pa	$10^5$	[20]
Diffusion coefficient of air in the extra-membrane medium	$D_{gl}$	$\text{m}^2\cdot\text{s}^{-1}$	$3.68\cdot 10^{-9}$	[27]
Effective thickness of boundary layer between extramembrane medium and intramembrane space for gas transport	$\xi$	nm	0.5	[11]
Vacuum permittivity	$\epsilon_0$	$\text{F}\cdot\text{m}^{-1}$	$8.854\cdot 10^{-12}$	[28]
Relative permittivity of the intramembrane cavity	$\epsilon_r$	-	1	[11]
Resting membrane capacitance	$C_{m0}$	$\mu\text{F}\cdot\text{cm}^{-2}$	1.0	[19]

### 2.1.2 NICE electrical model.

The electrical part of the NICE electromechanical model predicts that the alternating expansions and compressions of a cavitating sonophore induce local, periodic oscillations in the plasma membrane capacitance (given by  $C_m(Z) = \frac{C_{m0}\Delta}{a^2} \left[ Z + \frac{a^2 - Z^2 - Z\Delta}{2Z} \ln\left(\frac{2Z+\Delta}{\Delta}\right) \right]$  as in [11]), which in turn cause large-amplitude oscillations of the transmembrane potential  $V_m$  near the resonating structure. The detailed effects of such voltage variations on neuronal excitation are cell-type-specific and captured by a modified Hodgkin-Huxley differential system (Figure 1(b)), where the evolution of the local membrane potential  $V_m$  depends not only on the contribution of several ionic currents with specific conductances  $g_i$  and reversal potentials  $E_i$ , but also on a so-called capacitive displacement current ( $I_C = V_m \frac{dC_m}{dt}$ ) originating from the capacitance oscillations:

$$\begin{aligned} \frac{dV_m}{dt} &= -\frac{1}{C_m} \left[ V_m \frac{dC_m}{dt} + \sum_i g_i \cdot (V_m - E_i) \right] \\ \frac{dx}{dt} &= \begin{cases} \alpha_x(V_m) \cdot (1-x) - \beta_x(V_m) \cdot x \\ \frac{x_\infty(V_m) - x}{\tau_x(V_m)} \end{cases} \end{aligned} \quad (2)$$

In this system, non-leakage ionic conductances are regulated by the product of one or multiple gating variables  $x$ , whose evolution is regulated by specific voltage-dependent activation and inactivation rate constants ( $\alpha_x$  and  $\beta_x$ , respectively), or by a steady state probability  $x_\infty$  and a time constant  $\tau_x$  (also both voltage-dependent). Sodium ( $m$  and

h) and delayed rectifier potassium ( $n$ ) currents gating variables have been defined with the former paradigm [19], while that of slow non-inactivating ( $p$ ) and calcium ( $s$  and  $u$ ) currents are defined with the latter one [12,19].

It should be noted that the electric pressure term  $P_Q$  depends directly on the membrane charge density, and therefore varies over the course of neural activation. As a result, the mechanical and electrical differential systems are bidirectionally coupled.

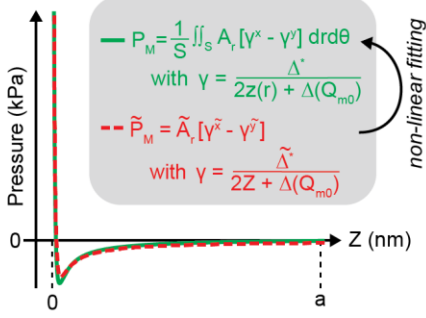
## 2.2 A multi-Scale Optimized Neuronal Intramembrane Cavitation (SONIC) model

The NICE mechanical model (described in [11]) and the Hodgkin-Huxley models of cortical regular spiking (RS), fast spiking, low-threshold spiking (LTS), thalamic reticular, and thalamo-cortical neurons (described in [12]), as well as Subthalamic Nucleus (STN) neurons (described in [29,30]) have been implemented in Python 3.6 and coupled together, using identical equations and parameters as in the references. Model equations are solved here with the *odeint* function from the *scipy.integrate* Python library (<http://www.scipy.org>) that uses a fixed step, variable order solver automatically selecting between nonstiff (Adams) and stiff (BDF) methods based on dynamic monitoring of the integrated system [31,32]. Numerical simulation of a RS neuron with typical sonophore in-plane radius (32 nm) and LIFUS parameters (500 kHz carrier frequency, 100 kPa pressure amplitude) reveals the extreme stiffness of the differential system. In consequence, the algorithm requires to use many time steps per acoustic period (1000 in our implementation) to ensure stable integration of intra-cycle system oscillations, and results in tremendous computation times ( $> 1$  day for a 150 ms CW stimulus). Therefore, we introduce here multiple optimization steps to reduce the computational cost of the algorithm.

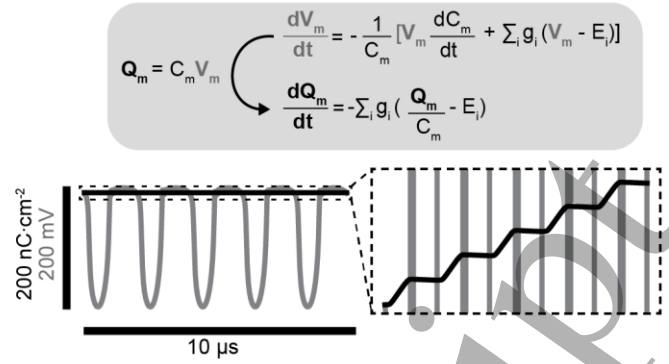
### 2.2.1 Lennard-Jones approximation of intermolecular pressure.

Profiled simulations of the mechanical model in isolation reveal that the spatial integration of intermolecular pressure  $P_M$  is by far the longest internal computation at each iteration. However, despite its complexity, this integrated pressure term depends solely on leaflet deflection and the nature of its profile is similar to that of its local counterpart. Therefore, a precomputing step is defined wherein a Lennard-Jones expression of the form  $\widetilde{P}_M(Z) = \widetilde{A}_r \left[ \left( \frac{\widetilde{\Delta}^*}{2Z + \Delta(Q_m)} \right)^{\widetilde{x}} - \left( \frac{\widetilde{\Delta}^*}{2Z + \Delta(Q_m)} \right)^{\widetilde{y}} \right]$  is fitted to the integrated profile and then used as a new predictor of intermolecular pressure during the iterative numerical resolution (Figure 2(a)). This simplification allows to reduce computation times by more than one order of magnitude, without significantly affecting the resulting deflection profiles (RMSE = 0.8% of cavitation extent over one acoustic period for typical simulation conditions mentioned above).

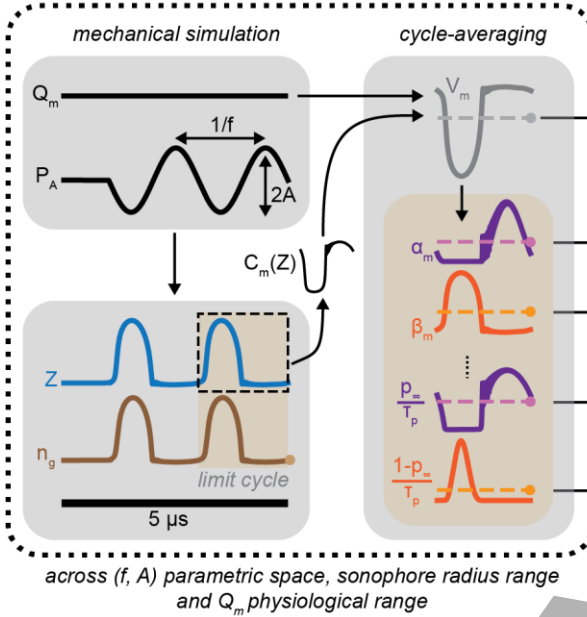


(a) *Lennard-Jones approx.*  
of intermolecular pressure

(b) recasting of electrical system



(c) precomputing



(d) hybrid integration

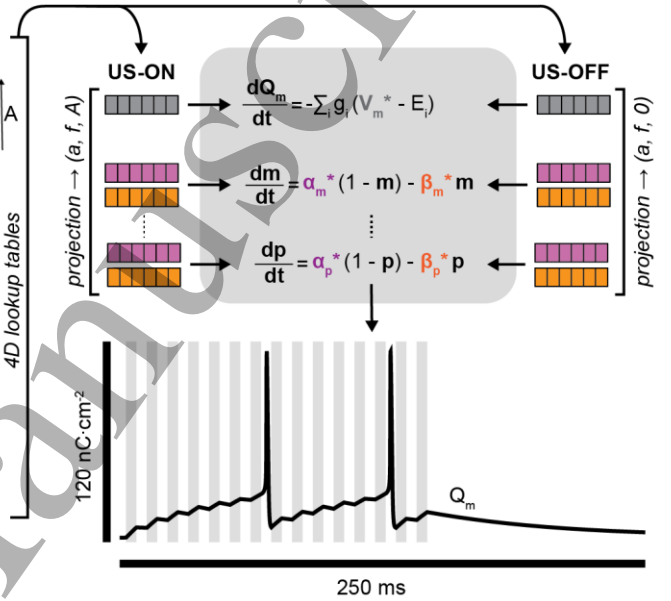


**Figure 2. Description of the model simplification and optimization steps.** (a) Comparison of spatially integrated (green) and fitted approximation (dashed red) of intermolecular pressure profiles for a realistic range of deflections. (b) Explicit representation of the electrical system recasting, along with a comparison of the short-term evolution of the membrane potential ( $V_m$ ) and charge density ( $Q_m$ ) upon sonication (500 kHz, 100 kPa), showing remarkably different stiffness. (c) Schematic representation of the coarse-graining and precomputing pipeline. Mechanical simulations are run until periodic stabilization of  $Z$  and  $n_g$ , at which point the membrane capacitance  $C_m$ , transmembrane potential and voltage-gated rate constants are computed over the last acoustic cycle. The average value of  $V_m$  and rate constants are then stored into lookup tables. The process is repeated for various combinations of sonophore radii ( $a$ ), US frequencies ( $f$ ), acoustic pressure amplitudes ( $A$ ) and membrane charge densities. (d) Schematic representation of the hybrid integration of the electrical system. Lookup tables are interpolated at a specific sonophore radius, US frequency and acoustic amplitude to yield 1D projected vectors of effective variables in the  $Q_m$  space, which are then used alternatively to interpolate effective variables during US-ON and US-OFF periods, respectively.

### 2.2.2 Recasting of the electrical system.

Simulations of the detailed NICE electromechanical model predict that while the local membrane potential of a cavitating sonophore undergoes large-amplitude oscillations, the membrane charge density and the ion channel gating variables around that structure evolve much more smoothly over the course of neural activation ([11] and Figure 2(b)). Therefore, the distinct electrical system is first recast as function of charge (using the transformation  $Q_m = C_m \cdot V_m$ ), thereby removing the capacitive displacement current term and yielding a new scheme composed only of smooth differential variables:



(3)

$$\begin{aligned} \frac{dQ_m}{dt} &= - \left[ \sum_i g_i \cdot \left( \frac{Q_m}{C_m} - E_i \right) \right] \\ \frac{dx}{dt} &= \begin{cases} \alpha_x \left( \frac{Q_m}{C_m} \right) \cdot (1 - x) - \beta_x \left( \frac{Q_m}{C_m} \right) \cdot x \\ \frac{x_\infty \left( \frac{Q_m}{C_m} \right) - x}{\tau_x \left( \frac{Q_m}{C_m} \right)} \end{cases} \end{aligned}$$

As  $Q_m/C_m$  is still rapidly oscillating, the evolution of electrical differential variables during US-ON periods is then expressed as a function of “effective” internal variables (using this time the rate constants formulation for all gates, with  $\alpha_x = x_\infty/\tau_x$  and  $\beta_x = 1/\tau_x - \alpha_x$ ), obtained by averaging their rapid oscillatory part over an acoustic period  $T$ . This is only possible because the differential variables evolve smoothly and allows to capture the millisecond-scale system evolution without explicitly resolving intra-cycle oscillations:

(4)

$$\begin{aligned} \left( \frac{dQ_m}{dt} \right)^* &= - \sum_i g_i \cdot \left( \frac{\int_0^T \frac{Q_m}{C_m(Z)} dt}{T} - E_i \right) \\ \left( \frac{dx}{dt} \right)^* &= \frac{\int_0^T \alpha_x \left( \frac{Q_m}{C_m(Z)} \right) dt}{\alpha_x^*} \cdot (1 - x) - \frac{\int_0^T \beta_x \left( \frac{Q_m}{C_m(Z)} \right) dt}{\beta_x^*} \cdot x \end{aligned}$$

We shall refer to  $V_m^*$  as the effective membrane potential and to  $\alpha_x^*$  and  $\beta_x^*$  as effective rate constants.

### 2.2.3 Precomputation and hybrid integration of effective solutions.

As they depend directly on the sonophore deflection profile and thus indirectly on the sonophore geometry, LIFUS parameters and electromechanical coupling, effective variables are precomputed for various combinations of sonophore radii ( $a$ ), US frequencies ( $f$ ), acoustic peak pressure amplitudes ( $A$ ) and membrane charge densities – covering the LIFUS parametric space, sonophore geometrical range and membrane physiological range – and then stored in 4D lookup tables to be linearly interpolated at runtime (Figure 2(c)). For each combination, a short simulation of the mechanical system is performed until a limit cycle is reached (detected by thresholding the root mean square error between two consecutive cycles of both  $Z$  and  $n_g$ ), and effective variables are then computed over the last acoustic cycle. The required granularity of lookup tables was determined by visually inspecting the nonlinearity of effective variables along each dimension. Lookups are computed here for 3 characteristic sonophore radii (16, 32 and 64 nm), 7 carrier frequencies (20, 100 and 500 kHz, 1, 2, 3 and 4 MHz), pressure amplitudes including 0 Pa and 50 logarithmically

distributed values between 0.1 and 600 kPa, and cell-type-specific ranges of physiologically realistic, linearly distributed charge densities (from  $V_{m0} \cdot C_{m0}$  - 25 to 50 nC/cm<sup>2</sup> with a 1 nC/cm<sup>2</sup> step).

Effective solutions are computed by interpolating effective variables at  $(a, f, A)$  and  $(a, f, 0)$  to yield 1D projected vectors in the  $Q_m$  space, which are then used to interpolate effective variables and solve equation (4) during US-ON and US-OFF periods, respectively (Figure 2(d)). The same *odeint* solver as for the detailed NICE model is used, however the absence of rapid oscillations allows to use a constant time step far greater than a typical acoustic period ( $dt = 50 \mu s$ ).

For the sake of simplicity, this new model variant involving electrical system recasting and coarse-graining, precomputation of effective variables and hybrid numerical integration using lookup interpolation tables will be referred to as SONIC model later on.

## 2.3 Comprehensive characterization of neural responses

### 2.3.1 Spike detection and derived metrics.

Incident neural spikes are detected on charge density profiles as local maxima using prominence thresholding, and neighboring local minima are used to define the spike boundaries. Spike amplitude is defined as the smallest differential between the local maximum and the neighboring local minima. Latency is defined as the delay between the stimulus onset and the occurrence of the first spike, and firing rate as the average of reciprocals of inter-spike intervals, accounting only for spikes occurring during the stimulus interval.

### 2.3.2 Systematic exploration of the LIFUS parameter space.

A typical LIFUS protocol comprises five distinct stimulation parameters: US frequency, acoustic peak pressure amplitude, pulse repetition frequency (PRF), duty cycle (DC), and duration, all of which substantially affect the mechanical and electrical response of a neuron. The latter also depends heavily on the cell-type-specific ion channel population and on the acoustic properties of the immediate anatomical environment. Hence, LIFUS optimization is a complex problem that requires the exhaustive characterization of the effects of multiple, possibly co-dependent, parameters over a high-dimensional space – a challenge that goes far beyond what is experimentally feasible. In this context, computational models can constitute a powerful tool to study the effect of a specific set of parameters in an isolated manner, provided they can be used efficiently.

The NICE electromechanical model predicts that cell-type-specific sensitivities to LIFUS can be classified into two main categories, depending on the presence or absence of a voltage-gated depolarization current active at sub-threshold charge levels [12]. Therefore, the parameter space is systematically explored for RS and LTS neurons – that provide a typical use case for each category – by varying the following stimulation parameters: sonophore radius (5 logarithmically distributed values from 16 to 64 nm), US frequency (500 kHz and 4 MHz), acoustic peak pressure

amplitude (30 logarithmically distributed values from 10 to 600 kPa), PRF (10, 100 and 1000 Hz) and duty cycle (1 to 100% with a 1% step). Stimulus duration is fixed to 1 s in order to analyze all relevant features of neural responses (excitation thresholds, firing rate adaptation, bursting behaviors, etc.). Two-dimensional behavior maps are then produced by plotting firing rates of resulting responses as a function of duty cycle and pressure amplitude, since neural activation across cell types is found to be mostly sensitive to these parameters, presumably along with the sonophore radius.

## 2.4 A multi-compartmental SONIC model to study spatially-distributed nanoscale interactions

Because it is recast as a differential system akin to the familiar Hodgkin-Huxley formulation, the SONIC model can be easily extended into multiple spatial compartments. Considering the inherent assumptions of the intramembrane cavitation theory, the first (most evident) expansion scale to consider is that of the sonophore itself, in interaction with its direct surroundings. Therefore, a nanoscale multi-compartmental SONIC model is developed to study the impact of that interaction on the local neural response. It consists of two radially symmetric membrane sections (Figure 3): a bilayer sonophore (compartment *S*) of radius *a*, surrounded by a LIFUS-insensitive circular membrane patch (compartment *I*) expanding from *a* to an outer radius *b*. The ratio of sonophore membrane area ( $\pi a^2$ ) divided by the total membrane area ( $\pi b^2$ ) is designated as the sonophore coverage fraction ( $f_s = a^2/b^2$ ). Compartments *S* and *I* are modeled electrically by voltage gated RC circuits, representing the local effective transmembrane dynamics of an RS neuron in the LIFUS-modulated sonophore region and the LIFUS-insensitive surrounding membrane. Both compartments are linked to ground in the extracellular medium, and connected to each other within a sub-membrane intracellular space of depth  $d_{eff}$  by a cylindrical resistor  $R_{SI}$ . The resistor value is approximated by considering an element that spans between the middle radial coordinates of compartments *S* and *I*, such that  $R_{SI} = \int_{\frac{a}{2}}^{\frac{a+b}{2}} \frac{\rho}{2\pi \cdot d_{eff} \cdot r} dr = \frac{\rho}{2\pi \cdot d_{eff}} \ln\left(\frac{a+b}{a}\right)$ , where the cytoplasmic resistivity  $\rho$  is set to the typical value of 100  $\Omega \cdot \text{cm}$  [35]. Finally,  $d_{eff}$  is arbitrarily set to 100 nm, i.e. within the order of magnitude of a typical sonophore diameter.

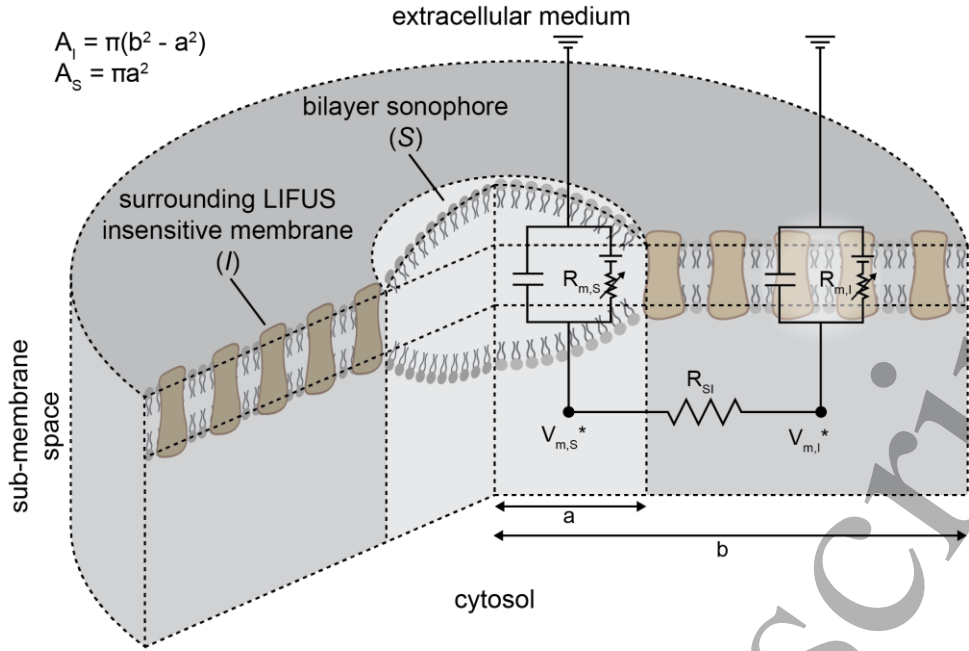


**Figure 3. Schematic representation of the nanoscale multi-compartmental SONIC model.** A bilayer sonophore of radius  $a$  ( $S$ , in light grey) is surrounded by a LIFUS-insensitive circular membrane patch ( $I$ , in dark grey) expanding between  $a$  and an outer radius  $b = a/\sqrt{f_s}$ , where  $f_s$  represents the sonophore coverage fraction of the total membrane area. Both sections are modeled electrically by voltage gated RC circuits, linked to ground in the extracellular medium, and connected to each other within a sub-membrane intracellular space of depth  $d_{eff}$  by a cylindrical resistor  $R_{SI}$ .

In this cylindrically geometric model, the effective variation of membrane charge density in each compartment results from (1) transmembrane currents triggered by the local effective membrane potential variations, and (2) effective intracellular currents between the two compartments as a result of differences in local effective membrane potential:

$$I_{SI}^* = \frac{1}{T} \int_0^T \frac{V_{mS} - V_{mI}}{R_{SI}} dt = \frac{V_{mS}^* - V_{mI}^*}{R_{SI}}. \text{ It results in the following equations:}$$

(5)

$$\left(\frac{dQ_{mS}}{dt}\right)^* = \frac{1}{\pi a^2} \cdot \frac{V_{mI}^* - V_{mS}^*}{R_{SI}} - \sum_i g_i \cdot (V_{mS}^* - E_i)$$

$$\left(\frac{dQ_{mI}}{dt}\right)^* = \frac{1}{\pi(b^2 - a^2)} \cdot \frac{V_{mS}^* - V_{mI}^*}{R_{SI}} - \sum_i g_i \cdot (V_{mI}^* - E_i)$$

where local ionic conductances are regulated by independent sets of gating variables defined as in equation (4).

This multi-compartmental model has been implemented *NEURON*[36], by using the precomputed lookup tables from an RS neuron (see Figure 2) to compute membrane currents, and a custom intracellular connection scheme explicitly casted in terms of  $V_m^*$  to compute intracellular currents.

The hypothesis of a unique, transmembrane potential variation across the entire membrane patch is also considered. This hypothesis was previously assessed with a point-like NICE model by only considering an attenuated version of the membrane capacitance oscillations resulting from the cavitating sonophore ( $C_m(t) = f_s \cdot C_{mS}(t) + (1 - f_s) \cdot C_{m0}$ ), thereby

reducing the variation range of the transmembrane potential [12]. Here, a point-like SONIC model is developed in parallel that uses lookup tables derived from mechanical simulations with this spatially averaged capacitance.

### 3. Results

#### 3.1 LIFUS-dependent effective variables

In this section, effective profiles of membrane capacitance, membrane potential and ion channels rate constants of an RS neuron are interpolated from the corresponding pre-computed lookup tables (see section 2.2.3 and Figure 2(c)) at various acoustic amplitudes, US frequencies, and sonophore radii, and evaluated as a function of membrane charge density.

##### 3.1.1 Effective membrane potential and rate constants are significantly amplified as a function of acoustic pressure amplitude.

In the absence of acoustic perturbation, the mechanical state of the sonophore is solely dependent on gas content and charge density. As the latter increases in magnitude, augmentation of the electrical pressure compresses the sonophore and increases its membrane capacitance. As a result, the profile of the unperturbed effective membrane potential  $V_m^* = Q_m/C_m$  is an odd function of  $Q_m$  that deviates slightly from linearity (Figure 4(a)). For small acoustic perturbations ( $A < 50$  kPa), the amplitude of intra-cycle oscillations is still heavily dependent on the electrical pressure. Hence, the sonophore expansions and the resulting capacitance drops throughout acoustic cycles are considerably reduced as the magnitude of membrane charge density increases. Thus, the effective membrane capacitance  $C_m^* = \left[ \frac{1}{T} \int_0^T \frac{dt}{C_m(Z)} \right]^{-1}$  displays an inverse bell-shaped profile as a function of charge, and the resulting effective membrane potential, despite conserving its odd symmetry, is amplified at intermediate values of  $|Q_m|$  before converging asymptotically towards its unperturbed counterpart as charge magnitude is further increased. Larger acoustic perturbations ( $A > 50$  kPa) induce greater sonophore expansions and capacitance drops within intra-cycle oscillations, during which the influence of the electrical pressure is heavily reduced. This means that the  $C_m^*$  profile is shifted towards lower values and exhibits little dependency on the charge density within the physiological range. Consequently, the  $V_m^*$  charge profile is amplified and transitions towards another quasi-linear regime. This amplification generates larger deviations from reversal potentials, and thus stronger ionic currents.

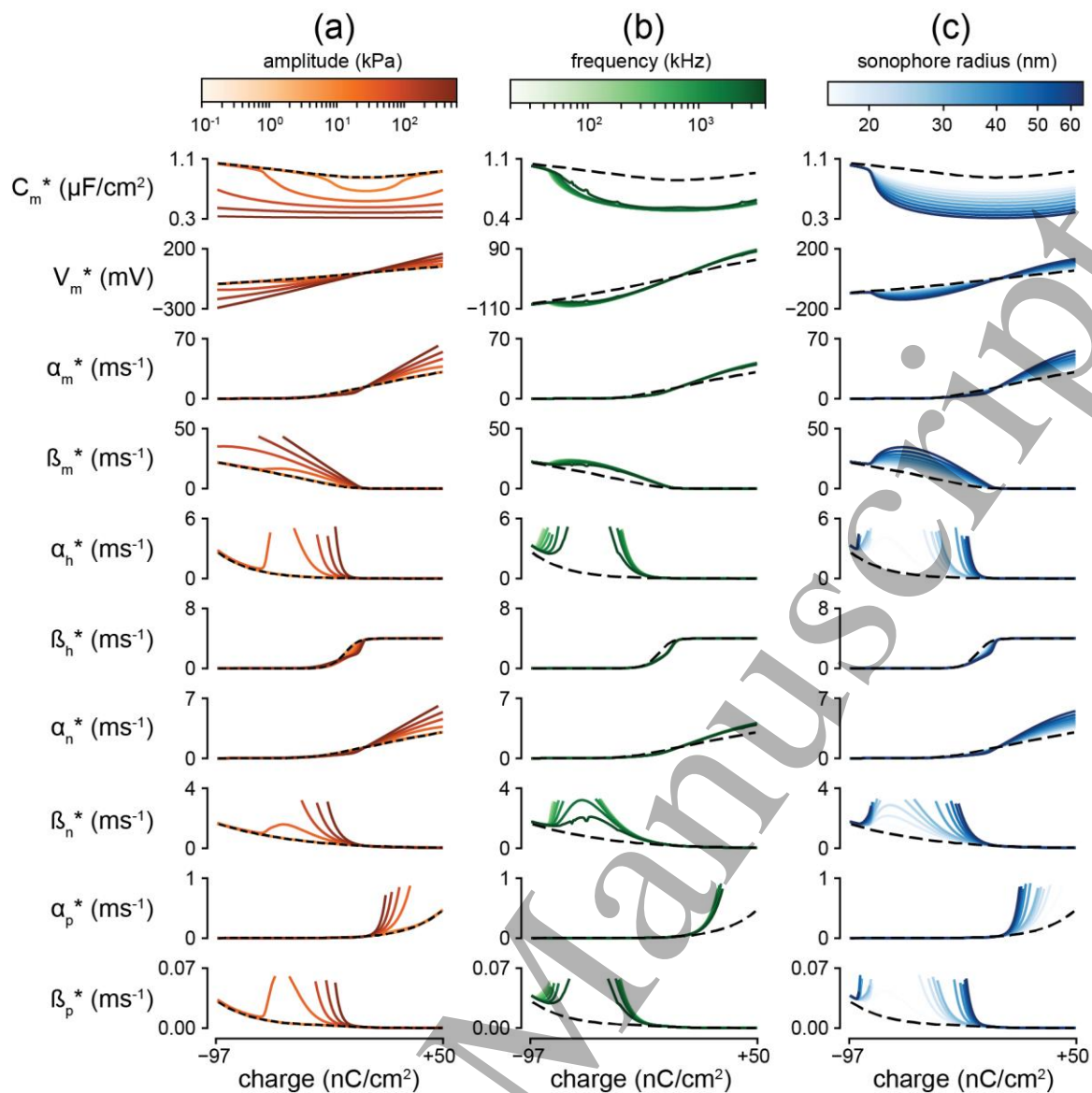


**Figure 4. Modulation of charge-dependent effective variables as a function of acoustic pressure amplitude, US frequency and intrinsic sonophore radius.** Effective variables of an RS neuron are displayed as a function of membrane charge density, with a color code corresponding to the modulating variable at which they were derived (color bar depicted on top). The original, non-modulated variables (dashed black lines) are also depicted for comparison. (a) Dependence on acoustic pressure amplitude (32 nm radius sonophore,  $f = 500$  kHz). (b) Dependence on US frequency (32 nm radius sonophore,  $A = 50$  kPa). (c) Dependence on intrinsic sonophore radius ( $f = 500$  kHz,  $A = 50$  kPa).

As voltage-gated rate constants are nonlinear functions of the membrane potential, their effective counterparts cannot be derived directly from  $V_m^*$  and must be explicitly computed. For small acoustic perturbations, they also deviate from their original counterpart at intermediate charge values and re-converge asymptotic towards it as we reach the borders of the physiological range. For large acoustic perturbations, all profiles are widely amplified around one extremity of the range due to their exponential nature, with the exception of the sigmoidal  $\beta_n$  profile. In particular,  $\alpha_m^*$  and  $\alpha_n^*$  are amplified for positive charge values which corresponds to faster openings of the sodium m-gate and potassium n-gate during action potentials. Hence, increasing acoustic amplitude also amplifies rate constants, which is likely to trigger faster gating variations.

### 3.1.2 Effective variables are significantly amplified as a function of the sonophore radius.

For intermediate values of acoustic pressure amplitude (here 50 kPa), varying the sonophore radius within a realistic range around its default value ( $16 < a < 64$  nm) produces significant changes in the effective variables profiles (Figure 4(b)). Expectedly, larger sonophores yield more pronounced sonophore expansions (as shown in [17]) and related capacitance drops, thereby amplifying the effective membrane potential profile in a charge-symmetric manner, as obtained when increasing acoustic amplitude. It results in a similar amplification of all effective rate constants. Oppositely, smaller sonophores have narrower periodic expansions, which limits the amplification of effective variables. The consequences of the dependence of effective variables on sonophore radius in terms of neuronal excitability are discussed in section 3.5.1.

## 3.2 Model validation

In this section, we evaluate the ability of the SONIC model to accurately reproduce membrane charge density profiles generated with the detailed NICE model (based on the charge-casted NICE electromechanical model described in equations (1) and (3)) for a variety of LIFUS conditions. For cases requiring the identification of sub- and supra-threshold regimes, a binary search to find the excitation threshold amplitude was conducted with the SONIC model and the appropriate neuron type, US frequency, and sonophore radius.

### 3.2.1 The model accurately captures predicted cell-type-specific excitation thresholds and responses to CW stimuli.

Under typical continuous-wave (CW) LIFUS conditions ( $f = 500$  kHz, 150 ms stimulus), the SONIC model accurately captures both passive responses of an RS neuron at sub-threshold amplitudes, and non-adaptive high-frequency tonic spike trains elicited at supra-threshold amplitudes (Figure 5(a), top). In the latter regime, amplitude-dependent variations in response latency, firing rate, and spike amplitude within the tonic train are picked up with a remarkable accuracy up to 600 kPa (Figure 5(a), bottom), a value far exceeding the pressure amplitudes used in recent neuromodulation studies on the CNS [37]. However, the model fails to capture the exact threshold amplitude at which the neuron transitions from a passive response to an active spiking behavior: integration with the detailed NICE model does not yield excitation at the threshold amplitude determined with the SONIC model (Figure 5(a), top). It can be assumed that this arises from the high nonlinearity of the effective membrane potential at low acoustic pressure amplitudes and negative charge densities (Figure 4(a)), yielding inaccurate linear interpolations during the build-up phase.



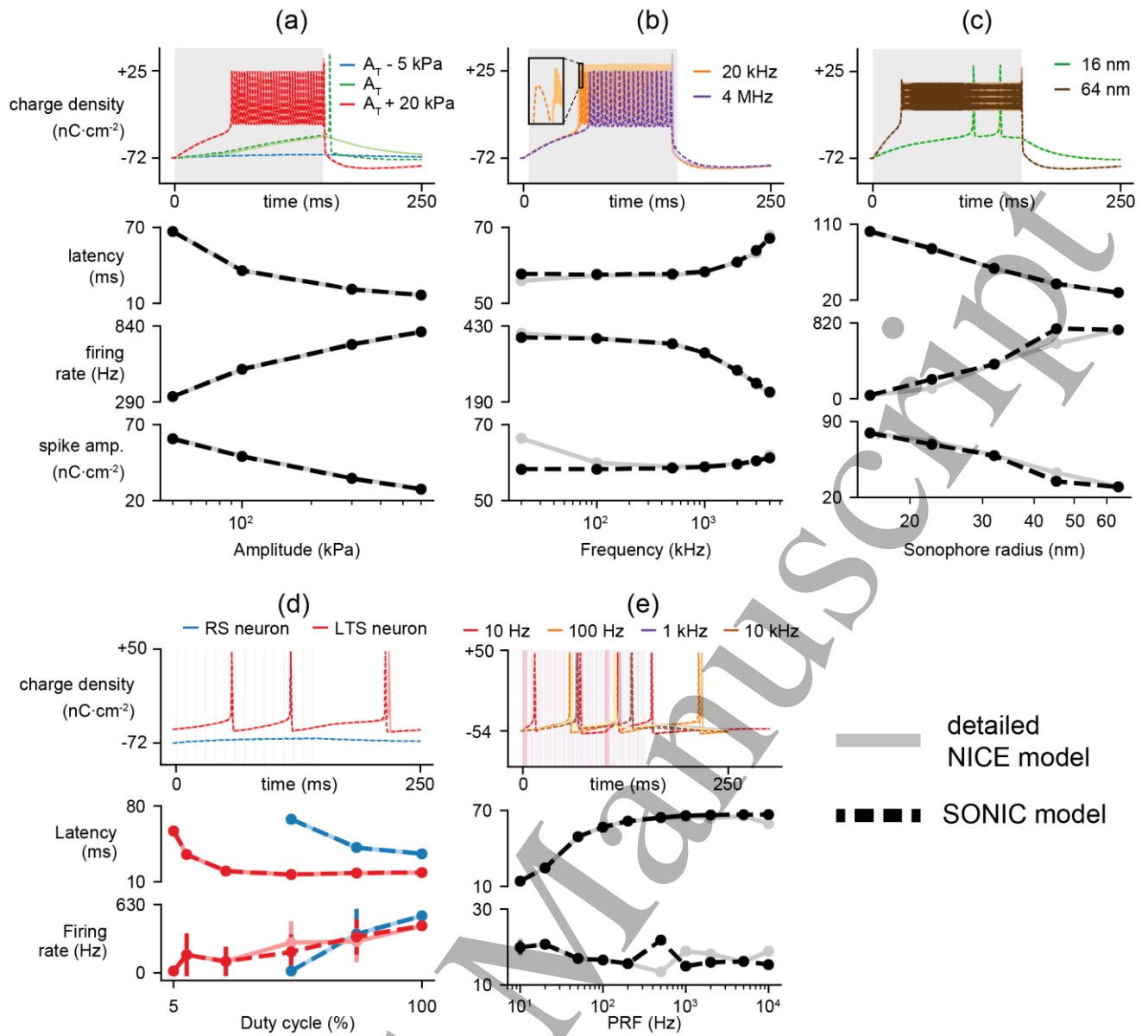


**Figure 5. Validation of the SONIC model against the detailed NICE model.** Membrane charge density profiles from simulations with the detailed NICE model (light solid curves) and SONIC model (dark dashed curves) of different neurons under various LIFUS conditions are compared, along with derived spiking metrics (latency, firing rate and spike amplitude). (a) Top: comparison of charge density profiles of a RS neuron under CW sonication ( $f = 500$  kHz) for sub-threshold ( $A_T - 5$  kPa), threshold ( $A_T$ ) and supra-threshold ( $A_T + 20$  kPa) acoustic pressure amplitudes. Bottom: comparison of derived spiking metrics for varying supra-threshold pressure amplitudes. (b) Top: comparison of charge density profiles of a RS neuron under CW sonication at supra-threshold amplitude (threshold + 20 kPa) with  $f = 20$  kHz and  $f = 4$  MHz. Bottom: comparison of derived spiking metrics for varying carrier frequencies from 20 kHz to 4 MHz. (c) Top: comparison of charge density profiles of a RS neuron under CW sonication at supra-threshold amplitude (threshold + 20 kPa) with 16 and 64 nm radius sonophores at  $f = 500$  kHz. Bottom: comparison of derived spiking metrics for varying sonophore radii from 16 to 64 nm. (d) Top: comparison of charge density profiles of RS (blue) and LTS (red) neurons under pulsed-wave (PW) sonication ( $f = 500$  kHz,  $A = 100$  kPa, 100 Hz PRF) at 5% DC. Bottom: comparison of derived spiking metrics for varying duty cycles from 5 – 100%. (e) Top: comparison of charge density profiles of a LTS neuron under PW sonication ( $f = 500$  kHz,  $A = 100$  kPa, 5% DC) with PRF of 10 Hz, 100 Hz, 1 kHz and 10 kHz. Bottom: comparison of derived spiking metrics for varying PRF from 10 Hz to 10 kHz.

The model accuracy for supra-threshold amplitudes is conserved as the carrier frequency increases up to several MHz (Figure 5(b), top). However, significant differences in spike amplitude (and to a lesser extent in latency and firing rate) appear as the frequency approaches the lower bound of the US domain (Figure 5(b), bottom). In fact, at such low frequencies, the order-of-magnitude of the intra-cycle oscillations dynamics approaches that of the gating kinetics of sodium and potassium ion channels, thereby inducing large intra-cycle gating variations that modulate the membrane

charge density at the US frequency and cause considerable oscillations in the detailed solution (Figure 5(b), inset). As can be expected, these oscillations are absent from the effective solution because of the intrinsic cycle-averaging strategy of the SONIC model, but the resulting spiking behavior stays qualitatively correct. This intra-cycle interference (and the resulting divergence) vanishes at frequencies higher than 100 kHz. This supra-threshold accuracy is also conserved for the sonophore radii bounding the lookup interval (16 and 64 nm): the larger radius yields similar reductions in latency and spike amplitude and increases in firing rate, and vice-versa (Figure 5(c), top). Interestingly, simulations of the SONIC model at intermediate radii that are not present in the lookup tables yield identical latencies than those obtained with the detailed NICE model, but higher firing rates and spike amplitudes (Figure 5(c), bottom). This inaccuracy suggests that while the effective membrane potential governing the initial charge build-up exhibits a rather linear dependency on the sonophore radius, effective rate constants depend nonlinearly on this variable, hence a higher resolution of the lookup tables in this dimension would be needed to produce quantitatively identical results. Nonetheless, spiking patterns stay qualitatively similar. Thus, the SONIC model can estimate cell-type-specific threshold excitation amplitudes with a precision in the order of kPa, and accurately captures the amplitude, frequency and sonophore radius dependencies of neural responses to CW stimuli. Note that these observations translate to other neuron types since they all share the same mode of interaction with CW stimuli (data not shown), except for the STN neuron type which was validated separately (see section 4.1.3).

### 3.2.2 The model accurately captures predicted cell-type-specific responses to PW stimuli.

Under typical PW stimulation conditions ( $f = 500$  kHz,  $A = 100$  kPa, 100 Hz PRF), the SONIC model accurately captures cell-type-specific, DC-dependent changes in latency and firing rate of RS and LTS neurons, which are good representatives of the two main types of sensitivities to pulsed LIFUS protocols according to predictions from the NICE model [12]. In particular, at very low duty cycles, both the passive response of a RS neuron and the sparse firing of a LTS neuron are accurately reproduced (Figure 5(d), top). In the latter case, a minor divergence is initiated and amplified during US-OFF periods, which is likely due to the great sensitivity of the charge-casted system to initial conditions of early depolarization phases as well as intrinsic differences in the computation of membrane capacitance between the NICE and SONIC models. This divergence is also found for the RS neuron that starts firing at 50% DC and yields small inaccuracies in the reported firing rates (Figure 5(d), bottom), despite producing very similar spiking behaviors. The SONIC model accuracy is mostly preserved throughout variations in PRF for a LTS neuron at 5% DC (Figure 5(e)), with two notable exceptions around 1 kHz and at 10 kHz. In the former case, the model inaccuracy is probably due to a particular pulse-spike synchronization that amplifies divergence of the effective solution – in fact, a slight divergence in the charge build-up phase can shift spike occurrence by one or several pulses, thereby offsetting the entire downstream response dynamics. In the latter case, however, divergence likely arises from the increasing number of ON-OFF transitions and the decrease of pulse duration down to the order of magnitude of the integration time step of the SONIC

model, limiting the number of iterations per pulse and thereby the accuracy of the effective solution. Thus, the SONIC model accurately captures the duty cycle and PRF dependencies of cell-type-specific neural responses to PW stimuli, relevant to different gating mechanisms.

### 3.3 The SONIC model boosts algorithmic efficiency by at least 3 orders of magnitude

The algorithmic acceleration provided by the presented SONIC model is assessed by comparing computation times of SONIC simulations with that of detailed NICE simulations, performed on the same computer (24-core, 2.1 GHz clock rate server, 126 GB RAM, Ubuntu 16.04.3 operating system).

For typical CW stimulation parameters ( $f = 500$  kHz), the detailed solution of the NICE model is computed in approx. 1 day, while the effective solution of the SONIC model is solved in less than 1 min. (Figure 6(a)), which corresponds to a gain in efficiency of more than 3 orders of magnitude.

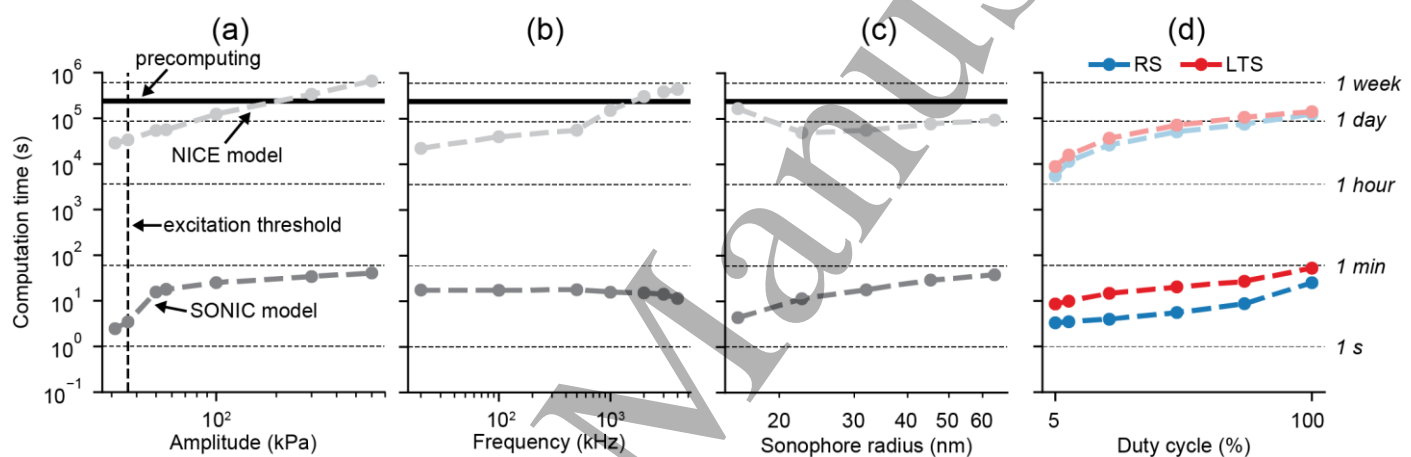


**Figure 6. Quantification of the SONIC model acceleration.** Comparison of computation times for 250 ms simulations under various LIFUS conditions, with the detailed NICE model (light gray) and SONIC model (dark gray, along with the fixed precomputation cost). (a) Comparison for CW simulations of the RS neuron at various sub- and supra-threshold acoustic amplitudes. The excitation threshold is also indicated (dashed vertical line). (b) Comparison for CW simulations of the RS neuron at various US frequencies with a supra-threshold amplitude (threshold + 20 kPa). (c) Comparison for CW simulations of the RS neuron with various sonophore radii, also at supra-threshold amplitude (threshold + 20 kPa). (d) Comparison for simulations of the RS (blue) and LTS (red) neurons ( $f = 500$  kHz,  $A = 100$  kPa, 100 Hz PRF) at various duty cycles. Dashed horizontal lines indicate characteristic durations.

The computation times of SONIC simulations show a significant increase between the sub- and supra-threshold regimes. This illustrates the stiffer differential system resulting from an active electrical response, as the employed LSODA solver uses an adaptive integration scheme that takes an increasing number of internal steps at each iteration as the system stiffness augments. Conversely, the computation times of NICE simulations augment linearly with acoustic amplitude and do not exhibit a sharp transition between those two regimes, as the full electromechanical model possesses a huge intrinsic stiffness that is hardly affected by the presence of an active electrical response, but rather by the increase in magnitude of intra-cycle oscillations.

Expectedly, computation times of the NICE model increase as the stimulus carrier frequency increases, owing to the algorithm's frequency-dependent integration time step, while those of the SONIC model do not exhibit any dependency

on that parameter (Figure 6(b)). The NICE model takes longer to compute supra-threshold simulations for very small sonophore radii – which could indicate an increase in the system’s nonlinearity for such small structures – and is otherwise rather constant across values of  $a$ . Conversely, the SONIC model takes longer to compute supra-threshold simulations (threshold + 20 kPa, where the threshold is determined for each value of  $a$  by a titration procedure) as the sonophore radius increases. This results from the greater sensitivity of larger sonophores to pressure amplitude, meaning that responses in the supra-threshold range transition faster towards tonic, high-frequency firing (see Figure 5(c)), which produces stiffer differential systems 20 kPa above the excitation threshold.

For PW stimuli, NICE computation times increase as the stimulus duty cycle increases, for both actively and passively responding neurons (Figure 6(d)), as a result of the longer LIFUS-ON total duration. SONIC computation times show less sensitivity to that parameter, but more intra-neuron variability: computation times for the actively responding LTS neuron are on average twice that of the RS neuron that is less activated, thereby confirming the influence of electrical variables on the effective system’s stiffness.

Overall, the gain in algorithmic efficiency provided by the SONIC model must be mitigated as it comes with an initial cost: the time required to inform the lookup tables necessary to run SONIC simulations is in the order of 2-3 days. However, this precomputation cost is fixed and can be significantly decreased by a trivial parallelization, which is impossible with the detailed NICE model.

### 3.4 Cell-type-specific excitability and spiking activity depends on multiple LIFUS parameters

The different sensitivities of the RS and LTS neurons to LIFUS have been previously characterized in [12]. This section aims at providing an interpretation of their respective recruitment mechanisms, based on the newly introduced effective membrane dynamics, and at using behavior maps to establish detailed trends of their firing behavior in different regions of the parameter space. It should be noted that a typical behavior map (i.e., 3000 simulations, see Methods section) was generated here in about 30 hours, a process that would have taken more than 10 years with the detailed NICE model.

#### 3.4.1 Regular spiking neurons are recruited by leakage currents above a critical ultrasonic dose.

In the sub-threshold state where the membrane charge density is below the neuron’s spiking threshold  $Q_T$ , LIFUS-ON periods of sufficient intensity trigger a strong effective hyperpolarization of several tens of millivolts that closes all voltage-gated ion channels, but also triggers a depolarizing leakage current (proportional to the difference  $V_m^* - E_{leak}$ ) that increases the membrane charge density (Figure 7(a), insets i-ii). At each pulse offset, the sudden mechanical stabilization of the membrane prompts an effective depolarization that crosses the leakage reversal potential and brings the membrane potential above its pre-pulse level, yet remaining in the sub-threshold state. Hence, the leakage current changes polarity and the charge density decreases. As a result, the net charge variation over a PRI depends on the

combination of pressure amplitude and duty cycle (referred to as US dose) that determines the magnitude and duration of LIFUS-ON effective depolarization, and is positive for US doses above a certain threshold. As the charge density progressively approaches  $Q_T$ , effective hyperpolarizations and depolarizations are shifted towards higher potential values, which diminishes the imbalance between the LIFUS-ON and LIFUS-OFF charge variations, ultimately reducing the net charge increase per PRI. Above a critical US dose, the imbalance stays positive as the charge crosses  $Q_T$ , at which point the sodium channels begin to open and drive further charge increase.

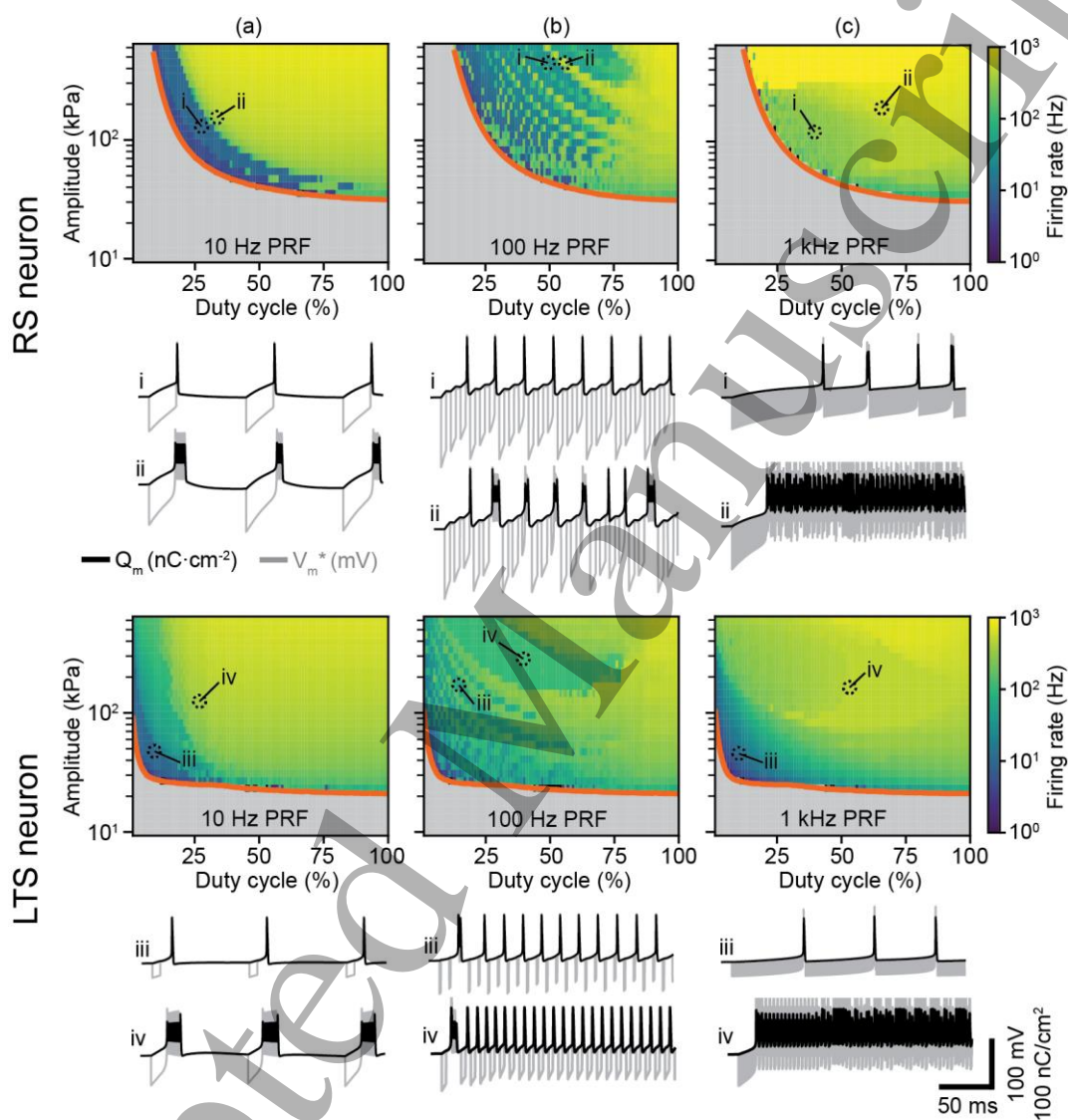


**Figure 7. Cell-type-specific LIFUS behavior maps.** Two-dimensional behavior maps depicting the firing rate of RS and LTS neurons (32nm sonophore radius, 500 kHz US frequency) as a function of duty cycle and amplitude, for various PRF, along with threshold excitation amplitudes predicted from titration procedures (orange curves). Temporal profiles of membrane charge density (black) and effective membrane potential (gray) are also depicted for selected combinations of duty cycle and amplitude. (a) Behavior maps and selected profiles at 10 Hz PRF. (b) Maps and profiles at 100 Hz PRF. (c) Maps and profiles at 1 kHz PRF.

### 3.4.2 Low-threshold spiking neurons can be recruited at lower ultrasonic doses thanks to calcium currents.

The LTS neuron is intrinsically easier to bring to a supra-threshold state due to its higher resting potential, and is thus generally activated at lower amplitudes than the RS neuron (Figure 7, bottom maps). Moreover, in the sub-threshold state, the sudden effective depolarization at pulse offsets triggers the transient opening of intrinsic low-threshold calcium

voltage-gated channels during LIFUS-OFF periods, producing a depolarizing current that can overcome the effect of the hyperpolarizing leakage current and drive further depolarization of the membrane towards  $Q_T$ . As a result, the LTS neuron can be excited at far lower duty cycles than the RS neuron with sub-MPa amplitudes (Figure 7(a), inset iii).

### 3.4.3 Cortical neurons can be entrained into different spiking behaviors depending on PRF values.

When a regular or low-threshold spiking neuron reaches the supra-threshold state ( $Q_m > Q_T$ ), the effective gating kinetics of sodium and potassium channels during LIFUS-ON periods trigger a high-frequency, non-adaptive train of action potentials with a high spiking frequency ( $> 100$  Hz) and reduced spike amplitude ( $< 70$  nC/cm<sup>2</sup>), as seen in Figure 5(a-c). During LIFUS-OFF periods, the system's behavior mainly depends on its electrical state at the preceding pulse offset: a decreasing membrane charge at the transition tends to induce repolarization, whereas an increasing membrane charge triggers further depolarization towards an action potential of "standard" amplitude through the traditional (i.e., unmodulated) membrane dynamics of the neuron.

For low PRFs allowing complete membrane repolarization between consecutive pulses, both neurons exhibit a similar, typical behavior (Figure 7(a)): US doses just above their respective excitation threshold see each pulse trigger exactly one spike (insets i and iii), whereas at higher doses each pulse necessarily triggers a burst of spikes (insets ii and iv). Notice that the transition between those spiking patterns is sharper for the RS neuron.

At intermediate PRFs that induce an accumulative depolarization effect between consecutive pulses, both neurons exhibit more complex spiking patterns (Figure 7(b)). Just above the excitation threshold, a large number of pulses is required to trigger a single spike. This number decreases as the US dose is increased. For particular US doses, the rate of sub-threshold charge increase is such that after multiple preceding pulses, the neuron's excitation threshold is reached exactly at the time of a pulse onset, such that a burst of spikes can be fired within the pulse, enriching the firing rate spectrum with a high-frequency component. Interestingly, because the RS neuron's leakage-driven sub-threshold build-up is quasi-linear, it synchronizes its bursting activity with a multiple of the PRI (referred to as nPRI-locked bursting) in a robust manner throughout the stimulus (Figure 7(b), inset ii). Moreover, this behavior is achieved at specific combinations of duty cycle and pressure amplitude seen as distinct stripes of higher firing rate on the behavior map, corresponding to different multiples of the PRI, and surrounded by regions of cyclic spiking activity (Figure 7(b), insets i and ii). This clustered pattern of nPRI-locked bursting cannot be obtained for the LTS neuron, because of the nonlinear, influence of the T-type calcium current on the sub-threshold charge build-up. However, as the latter current enhances sensitivity to LIFUS, the LTS neuron can synchronize its spiking activity with the stimulus by firing exactly one spike for each pulse at high US doses (Figure 7(b), inset iv). This behavior (referred to as PRI-locked spiking) is seen over a large region of the considered amplitude-DC space, (which suggests that it could be reliably elicited), something that is not obtained with the RS neuron for the range of considered acoustic amplitudes. When further raising the acoustic dose, both neuron types fire a burst of spikes at each pulse.



At high PRF for which PRI is in the order of magnitude of spike duration, synchronization phenomena do not occur and both neurons show less regular responses (Figure 7(c)). At low US doses slightly above their respective excitation threshold, both neuron fire sparse spikes at a variable rate (Figure 7(c), insets i and iii). At higher US doses, this high-frequency pulsing protocol tends to constrain the membrane charge density to a supra-threshold regime and yields very high firing rates for both neurons (Figure 7(c), insets ii and iv), similar to those obtained by continuous stimulation.

### 3.5 Excitation thresholds are sensitive to LIFUS parameters and sonophore geometry

Visual inspection of effective variables reveals the significant influence of both US frequency and sonophore radius on a neuron's effective electrical system (Figure 4(b-c)), and ultimately on its electrical response. Hence, this section analyzes the influence of these two parameters on excitation thresholds, assessed using titration procedures.

#### 3.5.1 Neuronal excitability shows substantial sensitivity to the sonophore radius.

For an RS neuron, augmenting the sonophore radius to twice its reference value (64 nm) induces larger cavitation that amplifies the effective membrane potential (Figure 4(c)) and the resulting leakage-driven sub-threshold depolarization, thereby shifting the excitation threshold significantly towards lower US doses (Figure 8(a), solid curves). This decrease is particularly important at low duty cycles (e.g., > 3-fold decrease from 180 to 45 kPa at 20% DC). Oppositely, diminishing the sonophore radius to half its reference value (16 nm) induces a tremendous increase in threshold amplitudes. Again, this augmentation is particularly marked at low duty cycles (e.g., > 5-fold increase from 110 to 600 kPa at 25% DC, below which it becomes impossible to excite the neuron with amplitudes in our lookup range). However, the augmentation is also substantial at high duty cycles (e.g., from 30 to 65 kPa at 100% DC).

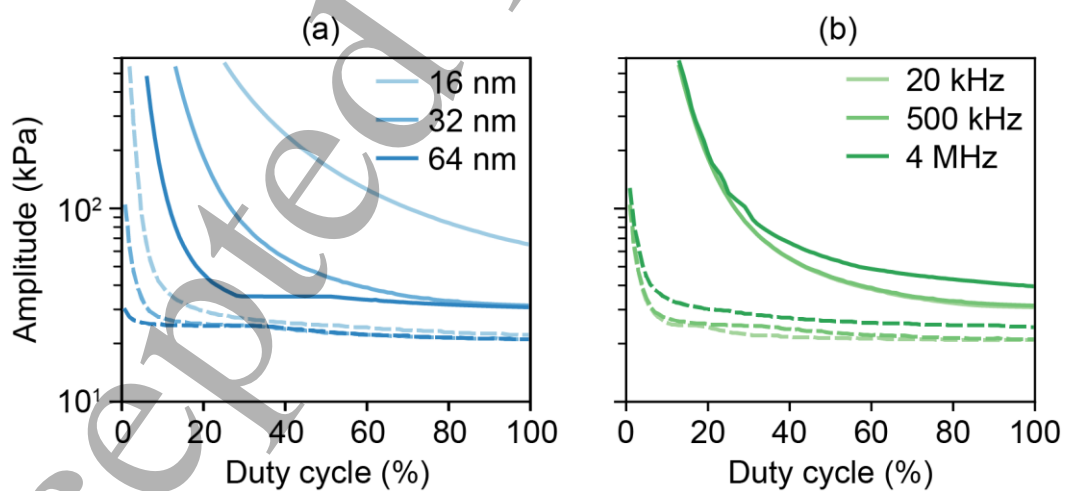


**Figure 8. Influence of sonophore radius and US frequency on excitation thresholds.** Threshold excitation amplitude as a function of the duty cycle for an RS neuron (solid curves) and an LTS neuron (dashed curves), predicted through titration procedures. (a) Effect of sonophore radius ( $f = 500$  kHz). (b) Effect of US frequency ( $a = 32$  nm).

The effects are smaller on an LTS neuron (Figure 8(a), dashed curves): doubling or halving the sonophore radius respectively shift the excitation threshold towards lower or higher US doses for small duty cycles (below 20% DC). For



larger duty cycles, the neuron's excitability is very robust to changes in sonophore extent (less than 5 kPa variation across the 3 conditions).

### 3.5.2 US frequencies above 1 MHz reduce neuronal excitability.

As anticipated from Figure 4(b), sub-MHz variations of the US frequency do not induce significant changes in the threshold excitation profiles of both neurons (Figure 8(b)). However, increasing the frequency up to 4 MHz induces stronger viscous stresses that limit the amplification of the effective membrane potential (Figure 4(b)) and the resulting leakage-driven sub-threshold depolarization, thereby shifting the excitation threshold towards slightly higher US doses. This effect is only relevant on large sonophores (here 32 and 64 nm radius) experiencing higher viscous stresses during cavitation. It is also more prominent in RS neurons than in LTS neurons, as the latter cell type is more dependent on LIFUS-ON periods to reach its spiking threshold.

## 4. Discussion

### 4.1 Interpretability of the SONIC model

#### 4.1.1 The SONIC model provides interpretability to the LIFUS-modulated spiking dynamics of cortical neurons.

The high degree of similarity between detailed and effective solutions of the NICE and SONIC electromechanical models, respectively, reveals that membrane charge density and ion channels gating variations during a LIFUS neural response can be expressed as a function of "effective" membrane potential and rate constants, averaged over acoustic cycles. These effective variables all exhibit a dependency on  $Q_m$  in the absence of acoustic perturbation, and they are amplified upon sonication to an extent that depends on acoustic pressure amplitude, US frequency and sonophore membrane span.

The amplification of effective variables explains key features of the specific dynamics observed in both cortical RS and LTS neurons during LIFUS-ON periods (Figure 5(a-c)). 1) Given that sodium and potassium have reversal potentials of opposite signs (50 and -90 mV, respectively),  $V_m^*$  amplification primarily increases the deviation from  $E_{Na}$  and thus the magnitude of the depolarizing sodium current when  $Q_m < 0$ , and deviation from  $E_K$  and the magnitude of the hyperpolarizing potassium current when  $Q_m > 0$ . This sign-dependent, ion-specific current amplification limits the charge density variation range, ultimately reducing the amplitude of the depolarization and hyperpolarization peaks reached during action potential trains. 2) The amplification of (i)  $\alpha_m^*$  and  $\alpha_n^*$  for positive charge densities and (ii)  $\beta_m^*$  and  $\beta_n^*$  for negative charge densities accelerate the opening and closing of the sodium and potassium activation gates during action potentials, further enhancing their temporal dynamics. 3)  $\alpha_n^*$  amplification triggers faster reactivation of the sodium  $h$ -gate upon repolarization, which effectively eliminates recovery periods between spikes, thereby considerably

increasing the firing frequency to a rate far superior to what can be evoked with electrical stimulation. 4)  $\alpha_p^*$  amplification accelerates the  $p$ -gate opening upon occurrence of the first spike, yielding a very fast firing rate adaptation within the first few spike intervals, and is therefore responsible for the non-adaptive nature of LIFUS-triggered spike trains. Hence, the SONIC model provides interpretability to the high-frequency and non-adaptive nature of spike trains in cortical RS and LTS neurons upon CW LIFUS.

#### 4.1.2 The SONIC model captures complex trends of LIFUS responses depending on multiple parameters.

Due to its associated computational burden, the NICE model only allows for sparse explorations of the LIFUS parameter space. While such explorations can reveal crucial information (e.g. cell-type-specific, DC-dependent excitation thresholds obtained by titration procedures), denser explorations such as the ones performed in this study allow to capture finer trends in neural responses, and to assess the influence of parameters such as the PRF on those trends. Here, we showed that low PRFs can entrain both neuron types into regular firing behaviors, transitioning from isolated spikes to cyclic bursting at the PRF as US doses are increased. Higher PRFs yield more complex behaviors, from dose-specific synchronization phenomena at 100 Hz to a more continuous interaction at 1 kHz.

#### 4.1.3 The SONIC model captures subtle neuromodulatory effects over narrow regions of the LIFUS space.

Interestingly, a recent computational study of the NICE model for STN neurons suggests that CW LIFUS can also induce other, subtle neuromodulatory effects on these spontaneously firing neurons [29]. Markedly, the authors predict that increasing levels of US doses successively elicit (1) steady increase in the firing rate of the neuron above its physiological baseline, (2) further increase of the firing rate with significant spike-frequency and spike-amplitude adaptation, and (3) generation of silenced plateau potentials after a transient period of adaptation. While those transitions between qualitatively distinct modes of LIFUS-neuron interaction occur over a narrow range of low acoustic amplitudes ( $A < 25$  kPa), they are remarkably captured by the SONIC model (Figure 9).

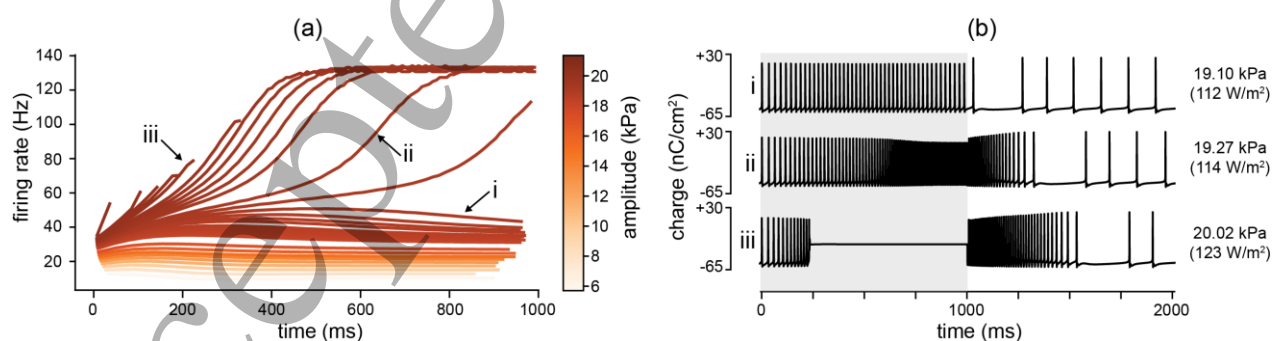


**Figure 9.** Distinct neuromodulatory effects of CW LIFUS ( $f = 500$  kHz) on STN neurons at very low intensities, as predicted by the SONIC model. (a) Temporal evolution of firing rate during LIFUS, defined as in [29], for increasing acoustic amplitudes. (b) Neural responses elicited at three specific amplitudes showing the distinct modes of interaction. Corresponding spatial peak pulse averaged intensities, computed as in [29] but with  $\rho_l = 1075$  kg·m<sup>-3</sup>, are shown for comparison. Electrical model parameters were taken from [29,30].

## 4.2 Effects of partial sonophore membrane coverage on neural responses

Sonophore membrane coverage is a key parameter of the NICE model likely to vary across a wide range of possible values. The influence of this parameter was previously assessed using a point-like NICE model with spatially-averaged capacitance, i.e. assuming that neural response is only sensitive to the spatial average of membrane potential variations. Here, instead, we assess the influence of partial sonophore membrane coverage using a nanoscale multi-compartmental SONIC model (see section 2.4) that considers the spatial co-distribution of sonophores with ion channels, as well as the effects of local intracellular currents, on an RS neuron's response.

For typical CW LIFUS parameters ( $f = 500$  kHz,  $A = 50$  kPa, 100 ms duration) and with 50% membrane coverage, the stimulus onset creates an instantaneous effective capacitance drop and hyperpolarization of the local sonophore membrane potential (Figure 10(a)). This creates an effective voltage imbalance with the unaffected surroundings, which drives significant intracellular currents. As these currents rapidly equilibrate the effective membrane potential across the 2 compartments, they also drive fast and significant changes in membrane charge density, increasing  $Q_m$  locally around the sonophore and decreasing it in the periphery. During the stimulus, the sonophore mechanical resonance induces leakage membrane currents that progressively increase the membrane charge density locally, but also in the periphery through the action of intracellular currents that equilibrate effective membrane potentials. After approximately 40 ms,  $Q_m$  around the sonophore eventually reaches the threshold value that drives the opening of local voltage-gated ion channels and triggers a spike train. As intracellular currents still maintain the  $V_m^*$  spatial equilibrium,  $Q_T$  is also reached in the surrounding membrane where voltage-gated ion channels also open. Both compartments then fire synchronized spike trains but with different  $Q_m$  variation ranges, since their effective electrical systems are not identically modulated by the stimulus. As the sonication stops, the sonophore membrane capacitance instantaneously returns to its resting value, which synchronizes charge density across the entire membrane patch.

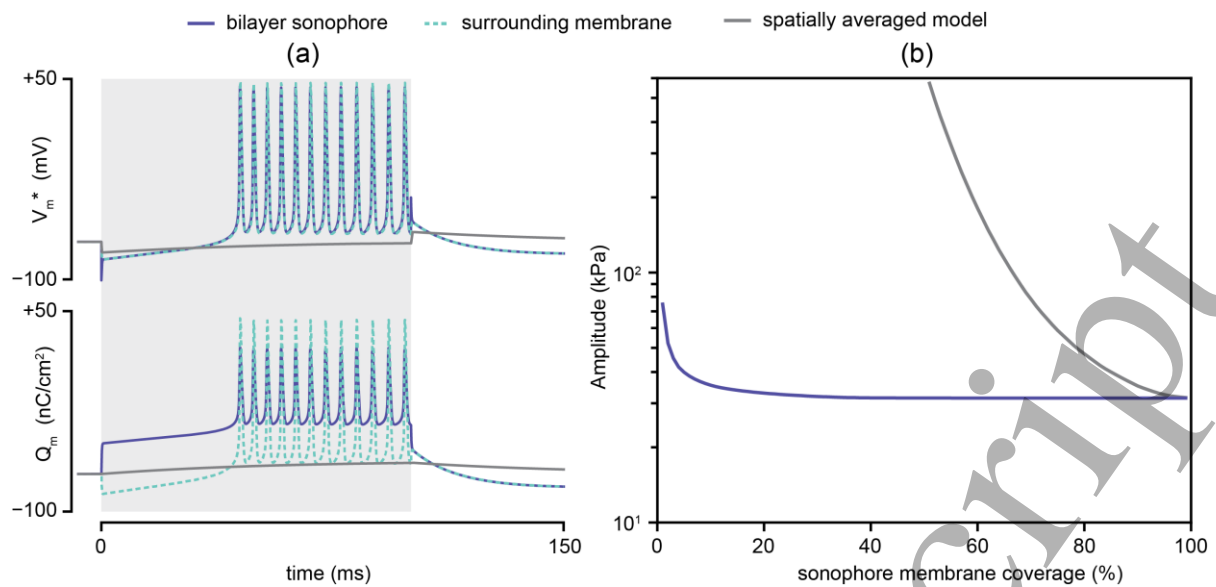


**Figure 10. Effects of partial sonophore membrane coverage on neural responses.** (a) Effective membrane potential (top) and charge density (bottom) of a RS neuron with 50% sonophore membrane coverage in response to CW sonication ( $f = 500$  kHz,  $A = 50$  kPa, 100 ms duration). Neural responses of a bilayer sonophore and its periphery computed with the nanoscale multi-compartmental SONIC model are depicted (solid dark and dashed light blue, respectively), as well the single response obtained with a point-like SONIC model using a spatially averaged membrane capacitance (grey). (b) Threshold excitation amplitude as a function of sonophore membrane coverage, computed with both the point-like (grey) and multi-compartmental SONIC (dark blue) models, using titration procedures at  $f = 500$  kHz (1 s stimulus).

This model involves several simplifications. First, it assumes that ion channels are present in the direct vicinity of a sonophore structure and respond to local changes in membrane potential, regardless of the global membrane fraction covered by such structures. Second, it assumes that these ion channels (in particular leakage channels) are present in sufficient number to drive a local depolarization up to the spiking threshold that may excite an entire neuron. Third, it neglects other intracellular driving forces that may be relevant at this nanometer scale, including the intracellular diffusion of ion particles following their concentration gradient. Fourth, it only consists of two compartments without further spatial discretization, and may therefore fail to capture the effects of a more continuous interaction between a sonophore and its surroundings. Fifth, it includes arbitrary choices such as the simplistic assumption of cylindrical symmetry, the value of effective sub-membrane depth and that of the intracellular resistor. Nevertheless, this model suggests that local depolarization around a sonophore generates intracellular currents that predominate overwhelmingly over membrane currents to synchronize the membrane electrical state in a very robust manner, unaffected by changes in key model parameters. In fact, while the choice of effective sub-membrane depth in this multi-compartmental model is indeed arbitrary, a sensitivity analysis shows that a decrease by several orders of magnitude below the nanometer range would be required in order to start observing desynchronized responses.

Critically, the point-like SONIC model considering a spatially-averaged potential across the entire membrane patch (see section 2.4) only predicts a sub-threshold response for identical parameters.

### 4.3 Influence of sonophore size and density on neural excitability

Simulations of the NICE model in reference studies [11,12] were all performed by assuming a constant sonophore radius of 32 nm – a value derived from the averaged distance between neighboring proteins in native oocytes [38]. While the order of magnitude of this parameter can be deemed reasonable, it is likely to vary significantly across organisms, cell types, and morphological sections of a given cell. Moreover, it is shown here that this parameter affects both the gating dynamics and the threshold excitation amplitudes of our neuron models, and is thus likely to play a key role in the excitability of most neuron types. In particular, it might shift the region of cortical suppression predicted in [12] to smaller or higher US doses.

Sonophore membrane coverage is another key variable likely to vary across a wide range of possible values. However, past simulations were mostly performed assuming 100% coverage, which is arguably unrealistic. The effect of partial coverage on neural response was only assessed for a single value of 75%, with a pressure amplitude far above the neuron's excitation threshold [12], using a point-like NICE model with a spatially-averaged capacitance. With this model, membrane charge density can only be brought above the spiking threshold by the progressive action of transmembrane depolarizing currents which, for an RS neuron under CW sonication, directly depend on the amplitude of LIFUS-triggered effective capacitance drop. As the sonophore membrane coverage decreases, the spatially-averaged drop is substantially dampened. This attenuates the effective variables of the electrical system, which raises excitation thresholds (Figure 10(b)). Under this paradigm, neuronal excitability is very sensitive to the density of sonophores: 75% coverage is enough to double the threshold excitation amplitude, and below 50% no pressure amplitude within the considered LIFUS range is able to excite the neuron.

The nanoscale multi-compartmental SONIC model – that considers spatially distributed voltage variations and ion channels gating – reveals an additional mechanism by which  $Q_m$  can be raised locally towards the spiking threshold. In fact, upon stimulus offset, the effective sonophore hyperpolarization generates local intracellular currents converging from the surrounding, unaffected membrane region that induce a rapid and substantial rise in the sonophore membrane charge density (Figure 10(a)). This effect is amplified for small fractions of sonophore coverage as the predominance of the unaffected membrane drives stronger intracellular currents towards the sonophore. However, this predominance also hinders the subsequent progressive charge increase once  $V_m^*$  has reached a spatial equilibrium. Nevertheless, this additional mechanism contributes to maintaining a very robust neuronal excitability as sonophore densities decreases (Figure 10(b)): excitation threshold amplitudes are hardly affected above 10%, and even a coverage fraction as low as 1% raises the threshold excitation amplitude by less than a factor 3.

The predicted effects of partial sonophore coverage on neural excitability are highly dependent on inherent model assumptions. The point-like SONIC model, considering spatially-averaged US effects on the membrane, predicts that

neuronal excitability is very sensitive to that parameter, and that low sonophore densities ( $f_s < 50\%$ ) may prevent the recruitment of cortical neurons with typical LIFUS protocols. Conversely, the multi-compartmental SONIC model developed here, considering spatially-distributed US effects on the membrane, predicts that the US excitability of cortical neurons is very robust to partial sonophore membrane coverage. More generally, the predictions of the latter model seem to agree with the experimental observation that US neuromodulation can be found in a diverse range of neural targets, despite important variabilities in their membrane structure. This observation suggests that the acoustic impact is likely to mechanistically interact with localized features of the structure (the sonophores in the case of the intramembrane cavitation hypothesis).

#### 4.4 Relevance for experimental validation

Despite predicting LIFUS parameter-dependent trends of neural activation and inhibition that match with indirect responses (e.g. hindlimb motor activity, mesoscale cortical activity) observed experimentally [11,12], one major limitation of the NICE electromechanical model is the lack of direct experimental validation at the cellular level, and in particular, direct observation of intramembrane cavitation, given the nanometer-scale extent of the hypothesized bilayer sonophores. Recording local oscillations in membrane thickness or transmembrane potential might be elusive, as this would require a sensing technology of high spatial ( $< 100$  nm) and temporal ( $\ll 1$   $\mu$ s) resolution with enough sensitivity to detect thickness variations of a few nanometers. However, the predicted dependency of excitation thresholds, response latencies, neural firing rates and spike amplitudes on LIFUS parameters are testable features that could (1) provide indirect validation of the NICE electromechanical hypothesis and (2) constrain specific model parameters with significant associated variability, such as the sonophore radius and density. In this context, our SONIC model defines effective membrane dynamics as a more interpretable frame of reference, supporting the design of such validation experiments and providing additional insight on how exactly LIFUS modulates ion channel gating dynamics.

#### 4.5 Generalizability and integration

The presented coarse-graining approach can be adapted to any neuron model with conductance-based membrane dynamics, provided that response time constants of its constituent voltage-gated ion channels are in the millisecond range. The translation into effective channel models could be further simplified by neglecting the small-scale changes in deflection profiles across different neuron types, and thus deriving cell-type-specific effective variables from a single precomputed table of mechanical deflections. Moreover, while we focused here on single neuron characterization, SONIC models of several neuron types could easily be coupled together with synaptic connections in order to design realistic, yet computationally efficient representations of cortical and/or peripheral neural networks responding to LIFUS. These network models could be used to increase our understanding of the influence of different LIFUS parameters on large-scale neural response as in [12]. Alternatively, they could guide the design of studies on the causal role of certain

brain regions in specific behaviors and behavioral disorders, as LIFUS currently emerges as very compelling technology for causal brain mapping [37].

#### 4.6 Advantage over other simplification strategies

The authors of the NICE electromechanical model have already proposed approaches to tackle the computational inefficiency of the original differential system (equations (1) and (2)), and speed up the numerical integration of solutions. A hybrid resolution scheme was developed that takes advantage of the weak influence of the electrical system on the mechanical one: the full electromechanical system is periodically integrated (every 500  $\mu$ s) for a few acoustic cycles until quasi-static (oscillatory) stabilization of the mechanical variables, which are then assumed to remain unchanged for the rest of the 500  $\mu$ s interval, allowing to integrate a simplified system with reduced stiffness for a large portion of the solution [11]. A later simplification was devised that represents the oscillations of sonophore membrane capacitance by a simple sinusoid at the US frequency, thereby dispensing from integrating the mechanical part of the model [12]. However, as both simplifications explicitly model the high-frequency, large-amplitude oscillations of the transmembrane potential, their integration time step must stay significantly smaller than the acoustic period to ensure convergence, which represents a strongly limiting factor for algorithmic optimization. Conversely, the time step used in our SONIC model is completely independent from the stimulus frequency, and only limited by the order of magnitude of the response time constants of constituent ion channels (as well as the PRI). Moreover, despite yielding excitation profiles that are qualitatively similar to that of the detailed NICE model, the sinusoidal capacitance-driven model does not properly capture the asymmetry of capacitance oscillations that dictates the dynamics of the initial charge build-up phase during CW stimulation; therefore, it cannot provide an accurate estimate of the response latency and excitation threshold for such protocols. On the other hand, our SONIC model considers this asymmetry during the precomputation of lookup tables, and can therefore reliably predict these excitation metrics. Obviously, this precomputation step is time consuming but it stays within the same order of magnitude as that required to run a single simulation of the detailed model. Moreover, it is a fixed cost, meaning one precomputation then allows to explore the entire parameter space. Furthermore, PRF and duty cycle do not need to be considered at this stage, which reduces the problem dimensionality. Finally, as it consists of a high number of small, independent mechanical simulations, precomputation can be easily optimized by parallelization (in fact, on our 24-core server, the parallelized process only takes 2 to 3 hours per neuron type).

## 5. Conclusion

In this study, we derived an effective coarse-grained variant of the NICE electromechanical model that greatly accelerates numerical simulations while preserving the accuracy of computed solutions and offering electrophysiological interpretability. This so-called SONIC model was used to explore systematically the LIFUS parametric space and



establish cell-type-specific behavior maps, by recasting LIFUS responses under the frame of an “effective” neural dynamics. We also expanded the SONIC model into a nanoscale multi-compartmental representation to study the impact of the electrical interactions between LIFUS receptive sub-cellular structures and their surroundings on the neural response. In ongoing work, we are conducting sonication experiments on isolated leech ganglia and analyzing the electrical responses of specific neurons to LIFUS with intracellular recordings, in order to verify the trends in effective spiking dynamics suggested by the model and provide indirect validation and quantification of the intramembrane cavitation mechanism. We are also expanding the SONIC model into cell-morphological neuron representations in order to study the effects of LIFUS on different neural structures in a more realistic manner.

## Acknowledgments

This work was partly funded by the Wyss Center for Bio and Neuroengineering (<https://www.wysscenter.ch/>) and by the Bertarelli Foundation (<https://www.fondation-bertarelli.org/>). The funders had no role in study design, data collection and analysis, decision to publish, or preparation of the manuscript. The authors have declared that no competing interests exist.

## References

- [1] Escoffre J-M and Bouakaz A 2016 *Therapeutic ultrasound*
- [2] Kyriakou A, Neufeld E, Werner B, Paulides M M, Szekely G and Kuster N 2014 A review of numerical and experimental compensation techniques for skull-induced phase aberrations in transcranial focused ultrasound *Int. J. Hyperthermia* **30** 36–46
- [3] Ghanouni P, Pauly K B, Elias W J, Henderson J, Sheehan J, Monteith S and Wintermark M 2015 Transcranial MRI-Guided Focused Ultrasound: A Review of the Technologic and Neurologic Applications *Am. J. Roentgenol.* **205** 150–9
- [4] Deffieux T, Younan Y, Wattiez N, Tanter M, Pouget P and Aubry J-F 2013 Low-intensity focused ultrasound modulates monkey visuomotor behavior *Curr. Biol. CB* **23** 2430–3
- [5] Kim H, Park M Y, Lee S D, Lee W, Chiu A and Yoo S-S 2015 Suppression of EEG visual-evoked potentials in rats through neuromodulatory focused ultrasound *Neuroreport* **26** 211–5
- [6] King R L, Brown J R, Newsome W T and Pauly K B 2013 Effective parameters for ultrasound-induced in vivo neurostimulation *Ultrasound Med. Biol.* **39** 312–31
- [7] Legon W, Sato T F, Opitz A, Mueller J, Barbour A, Williams A and Tyler W J 2014 Transcranial focused ultrasound modulates the activity of primary somatosensory cortex in humans *Nat. Neurosci.* **17** 322–9
- [8] Mueller J, Legon W, Opitz A, Sato T F and Tyler W J 2014 Transcranial focused ultrasound modulates intrinsic and evoked EEG dynamics *Brain Stimulat.* **7** 900–8
- [9] Tyler W J, Tufail Y, Finsterwald M, Tauchmann M L, Olson E J and Majestic C 2008 Remote Excitation of Neuronal Circuits Using Low-Intensity, Low-Frequency Ultrasound *PLOS ONE* **3** e3511
- [10] Younan Y, Deffieux T, Larrat B, Fink M, Tanter M and Aubry J-F 2013 Influence of the pressure field distribution in transcranial ultrasonic neurostimulation *Med. Phys.* **40** 082902
- [11] Plaksin M, Shoham S and Kimmel E 2014 Intramembrane Cavitation as a Predictive Bio-Piezoelectric Mechanism for Ultrasonic Brain Stimulation *Phys. Rev. X* **4**

- [12] Plaksin M, Kimmel E and Shoham S 2016 Cell-Type-Selective Effects of Intramembrane Cavitation as a Unifying Theoretical Framework for Ultrasonic Neuromodulation *eNeuro* **3**
- [13] Kim H, Taghados S J, Fischer K, Maeng L-S, Park S and Yoo S-S 2012 Noninvasive transcranial stimulation of rat abducens nerve by focused ultrasound *Ultrasound Med. Biol.* **38** 1568–75
- [14] Kim H, Chiu A, Lee S D, Fischer K and Yoo S-S 2014 Focused Ultrasound-mediated Non-invasive Brain Stimulation: Examination of Sonication Parameters *Brain Stimulat.* **7** 748–56
- [15] Tufail Y, Yoshihiro A, Pati S, Li M M and Tyler W J 2011 Ultrasonic neuromodulation by brain stimulation with transcranial ultrasound *Nat. Protoc.* **6** 1453–70
- [16] Yoo S-S, Bystritsky A, Lee J-H, Zhang Y, Fischer K, Min B-K, McDannold N J, Pascual-Leone A and Jolesz F A 2011 Focused ultrasound modulates region-specific brain activity *NeuroImage* **56** 1267–75
- [17] Krasovitski B, Frenkel V, Shoham S and Kimmel E 2011 Intramembrane cavitation as a unifying mechanism for ultrasound-induced bioeffects *Proc. Natl. Acad. Sci. U. S. A.* **108** 3258–63
- [18] Plesset M S 1949 The Dynamics of Cavitation Bubbles *J. Appl. Mech.* **16** 277–82
- [19] Pospischil M, Toledo-Rodriguez M, Monier C, Piwkowska Z, Bal T, Frégnac Y, Markram H and Destexhe A 2008 Minimal Hodgkin-Huxley type models for different classes of cortical and thalamic neurons *Biol. Cybern.* **99** 427–41
- [20] Wong H Y 1977 *Handbook of essential formulae and data on heat transfer for engineers* (London ; New York: Longman)
- [21] Boal D 2012 *Mechanics of the Cell* (Cambridge, UK ; New York: Cambridge University Press)
- [22] IT'IS Foundation 2015 Tissue Properties Database V3.0
- [23] Phillips R, Ursell T, Wiggins P and Sens P 2009 Emerging roles for lipids in shaping membrane-protein function *Nature* **459** 379–85
- [24] Rawicz W, Olbrich K C, McIntosh T, Needham D and Evans E 2000 Effect of chain length and unsaturation on elasticity of lipid bilayers. *Biophys. J.* **79** 328–39
- [25] Sun R, Hu W and Duan Z 2001 Prediction of Nitrogen Solubility in Pure Water and Aqueous NaCl Solutions up to High Temperature, Pressure, and Ionic Strength *J. Solut. Chem.* **30** 561–73
- [26] GENG M and DUAN Z 2010 Prediction of oxygen solubility in pure water and brines up to high temperatures and pressures *Geochim. Cosmochim. Acta* **74** 5631–40
- [27] Wise D L and Houghton G 1966 The diffusion coefficients of ten slightly soluble gases in water at 10–60°C *Chem. Eng. Sci.* **21** 999–1010
- [28] Mohr P J, Taylor B N and Newell D B 2008 CODATA recommended values of the fundamental physical constants: 2006 Rev. *Mod. Phys.* **80** 633–730
- [29] Tarnaud T, Joseph W, Martens L and Tanghe E 2018 Computational Modeling of Ultrasonic Subthalamic Nucleus Stimulation *IEEE Trans. Biomed. Eng.*
- [30] Otsuka T, Abe T, Tsukagawa T and Song W-J 2004 Conductance-Based Model of the Voltage-Dependent Generation of a Plateau Potential in Subthalamic Neurons *J. Neurophysiol.* **92** 255–64
- [31] Petzold L 1983 Automatic Selection of Methods for Solving Stiff and Nonstiff Systems of Ordinary Differential-Equations *Siam J. Sci. Stat. Comput.* **4** 136–48
- [32] Hindmarsh A C 1983 ODEPACK, A Systematized Collection of ODE Solvers *Scientific Computing* (Amsterdam) pp 55–64
- [33] Destexhe A, Contreras D, Steriade M, Sejnowski T J and Huguenard J R 1996 In vivo, in vitro, and computational analysis of dendritic calcium currents in thalamic reticular neurons *J. Neurosci. Off. J. Soc. Neurosci.* **16** 169–85

1 [34] Destexhe A, Neubig M, Ulrich D and Huguenard J 1998 Dendritic low-threshold calcium currents in thalamic relay  
2 cells *J. Neurosci. Off. J. Soc. Neurosci.* **18** 3574–88

3 [35] McNeal D R 1976 Analysis of a model for excitation of myelinated nerve *IEEE Trans. Biomed. Eng.* **23** 329–37

4 [36] Hines M L and Carnevale N T 1997 The NEURON simulation environment *Neural Comput.* **9** 1179–209

5 [37] Kubanek J 2018 Neuromodulation with transcranial focused ultrasound *Neurosurg. Focus* **44** E14

6 [38] Pralle A 1998 *Physical Properties of the Plasma Membrane Studied by Local Probe Techniques*